Coupling potential and viscous flow models with domain decomposition for wave propagations

Wen-jie Zhong[1], Wen-tao Wang[1, 2], De-cheng Wan[1*]
1. *Computational Marine Hydrodynamics Lab (CMHL), School of Naval Architecture, Ocean and Civil Engineering, Shanghai Jiao Tong University, Shanghai 200240, China*
2. *China Ship Scientific Research Center, Wuxi 214082, China*

Abstract: Either potential flow or viscous flow based model may be flawed for numerical wave simulations. The two-way coupling of potential and viscous flow models with the domain decomposition utilizing respective strengths has been a trending research topic. In contrast to existing literatures in which closed source potential models were used, the widely used open source OceanWave3D, OpenFOAM-v2012 are used in the present research. An innovative overlapping two-way coupling strategy is developed utilizing the ghost points in OceanWave3D. To guarantee computational stability, a relaxation zone used both for outlet damping and data transfer is built over the overlapping region in OceanWave3D. The free surface elevation in the relaxation zone is directly probed in OpenFOAM while the velocity potential is indirectly built upon its temporal variation which is calculated by the free surface boundary condition using the probed velocity. Strong coupling is achieved based on the fourth-order Runge-Kutta (RK) algorithm. Both two- and three-dimensional tests including linear, nonlinear, irregular, and multi-directional irregular waves, are conducted. The effectiveness of the coupling procedure in bidirectional data transfer is fully demonstrated, and the model is validated to be accurate and efficient, thus providing a competitive alternative for ocean wave simulations.

Key words: Domain decomposition, numerical wave tank, potential/viscous flow coupling, irregular waves, wave-structure interaction

Introduction

A challenge in the research of offshore applications is the accurate numerical reproduction of the wave fields. Waves from linear to extreme range advance towards structures randomly, near which wave breaking and vortex production occur leading to a viscous dominant regional flow field. The strategies to simulate waves fall into two classes, i.e., models based on the irrotational and inviscid flow assumption and the real fluid flow. The potential flow model arises due to its conciseness in mathematical formulation and efficiency in computation. A numerical method used in the potential flow model is the boundary element method (BEM)[1]. However, the efficiency of the potential flow model achieves at the sacrifice of accuracy and range of application, which poses great restrictions on the development of potential flow models. For example, severe wave scenarios involving flow rotation and overturning are out of the potential flow range. On the contrary, the viscous flow model deals with the complete conservation equations, allowing and controlling nonlinearities in the flow. Thus, arbitrary water surface evolutions can be captured or tracked using a proper choice of free surface treatment models, e.g., volume of fluid (VOF) model and level set (LS) method. The viscous flow model implemented in the framework of the computational fluid dynamics (CFD) has been broadly investigated in terms of wave generation and absorption[2-7]. Theoretically, the viscous flow model with fine mesh resolutions can obtain results infinitely close to the analytical solution, but limitations over the computational resources force a balance between accuracy and efficiency.

Recently, combining the potential and viscous flow models with the aim of utilizing the individual strengths has been a trending research topic. The model combination realizes through decomposition in either flow field or computational domain. The flow field decomposition, or the spectral wave explicit

Biography: Wen-jie Zhong (1990-), Male, Ph. D.,
E-mail: zhongwenjie@sjtu.edu.cn
Corresponding author: De-cheng Wan,
E-mail: dcwan@sjtu.edu.cn

Navier-Stokes equations (SWENSE) method, was originally applied in single-phase condition with the idea of dividing the wave solution into incident and perturbed parts evaluated by a dedicated potential flow model and a viscous flow model respectively[8-9]. The first attempt to two-phase SWENSE employed only partial flow variable decomposition in which the LS was used for tracking the free surface[10]. A thorough flow field decomposition in two-phase context was then accomplished using a modified Euler equation[11]. The superiority of the SWENSE over the viscous flow model lies in the fact that since the explicitly imposed incident wave field is unaffected by the mesh resolution, a wise mesh distribution with coarse mesh in the far-field region and fine mesh in the intense disturbance region near the structure can gain considerable computational savings.

The more widely studied combination or coupling of potential and viscous flow models is the domain decomposition. The value of this coupling is embodied in the nature of the wave field around structures that severe wave phenomena occur only near the structure while the far-field region is characterized by gentle wave motions which fulfill the potential flow assumption. Efficient numerical computations achieve when the intense wave domain at the proximity of the structure is simulated by a viscous flow model and the rest of the domain is simulated by a potential flow model. Conceptually, the coupling can occur in unidirectional and bidirectional manners known as the one-way and two-way coupling respectively. But it is considered that the one-way coupling is functionally the same as the individual viscous flow model except for the inlet boundary condition which is replaced by input from the coupled potential flow model. Recent examples of one-way coupling practices are Choi et al.[12], Gatin et al.[13], Paulsen et al.[14] and Zhuang and Wan[15]. The two-way coupling featured by bidirectional data transfer is truly domain decomposition. Many researches on different strategies of two-way coupling have been conducted. Iafrati and Campana[16] studied the two-way viscous-inviscid coupling between vertically decomposed domains for a submerged moving object. Two strategies characterized by overlapping and non-overlapping for coupling the upper viscous free surface domain and the lower inviscid object domain were compared. Iafrati and Campana[16] indicated that both coupling strategies can give satisfactory results but the overlapping strategy exhibits a smaller error. The vertical domain decomposition may be inferior since wave generation and absorption are necessary in both domains. The two-way coupling implemented in the horizontal domain decomposition with a single connecting boundary was studied by Zhang et al.[17], Zhang et

al.[18]. Zhang et al.[17] found that using the strong coupling with implicit time integration for matching water surface elevation at the connecting boundary results in more accurate surface elevation than the weakly coupled explicit time integration. Colicchio et al.[19] developed a two-way coupling procedure for horizontally overlapped domains and gave details on the data conversion between the potential and viscous flow models to be consistent with the receiver model. Colicchio et al.[19] also pointed out that the two-way coupling without overlapping appears less robust than that with overlapping and requires more stringent care on the discretization near the mutual boundary. Kim et al.[20] presented a simple two-way coupling with overlapping between a nonlinear BEM model and a viscous flow model, and concluded that the width of the overlapping zone is not a critical factor for the simulated surface elevation and 10% to 15% of the wave length was recommended for the overlapping width. In the horizontal domain decomposition in Hamilton and Yeung[21], the domain is divided into the interior cylindrical region linked to a viscous flow model and the exterior region linked to a linearized potential flow model, and a generalized three-dimensional two-way coupling across the cylindrical matching boundary was proposed. Besides, the domain decomposition approach permitting multi-physics simulations was also applied in coupling different viscous flow models, e.g., Ferrer et al.[22], Di Paolo et al.[23-24].

For interests of the present research, the two-way coupling with overlapping is considered. As reviewed above, most the existing strategies used closed source BEM model for performing the coupling[17-20]. In this research, the open source potential flow model OceanWave3D is adopted according to the performance comparisons among SWASH[25], OceanWave3D[26] and HOS-NWT[27] in Duz et al.[28], and is coupled with the open source viscous flow model OpenFOAM-v2012. An innovative two-way coupling strategy for combining the two codes is proposed. The new strategy utilizes the ghost points in OceanWave3D for converting kinematic data from OpenFOAM to OceanWave3D avoiding the velocity potential calculation step. Besides, a relaxation zone is built near the outlet in the OceanWave3D domain for prescribing the free surface elevation and velocity probed in OpenFOAM to secure computational stability. The velocity potential in the relaxation zone is evaluated from its temporal variation which is calculated by the free surface boundary condition equation using the probed velocity data. To validate the strategy, both two- and three-dimensional test cases, including regular, irregular, and multi-directional irregular waves, are conducted. Specific topics regarding the inclusion of turbulence model and

computational efficiency of the two-way coupling model are discussed. Moreover, applications of the coupling method to two wave-structure interaction problems against experiments have been carried out to further validate the model. Results show that the developed coupling strategy is robust in terms of accuracy and stability, and true domain decomposition is achieved via the effective and efficient two-way data transfer.
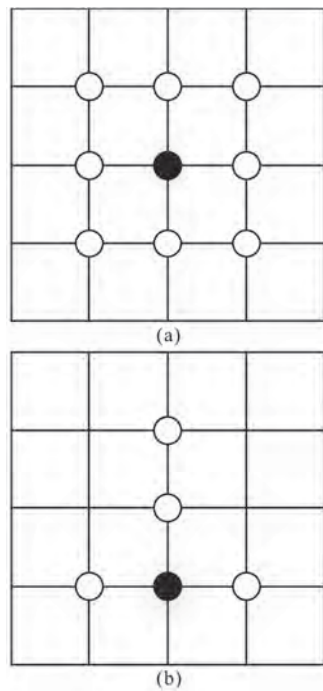

Fig. 1 Two-dimensional FDM discretization for internal and boundary points: (a) Centered stencil at the internal point for discretizing the Laplace equation, (b) Off-centered stencil at the boundary point for discretizing the boundary condition equation. The solid point is the point of interest and the hollow points constitute the computational stencil. The black thick line represents the boundary

The remainder of the paper is organized as follows: The potential and viscous flow models are given in the next section. The new two-way coupling strategy is described in Section 3. The validation test settings and results are provided in Section 4, and topics relating to the utility of the two-way coupling model, i.e., inclusion of turbulence model and efficiency, are also discussed. Then in Section 5, the coupling model is applied to two wave-structure interaction problems against published experiments. Finally, the conclusions are made in Section 6.

1. Numerical models

1.1 *Potential flow model*

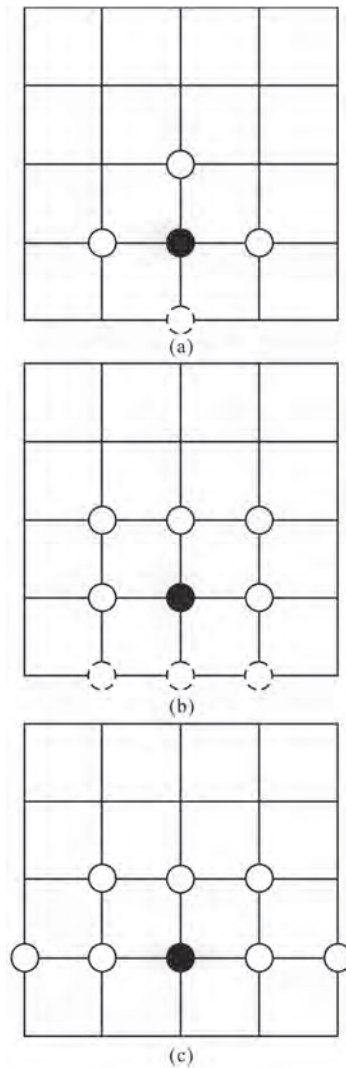The fully nonlinear potential flow model imple-

Fig. 2 Two-dimensional FDM discretization for boundary points in OceanWave3D: (a) Centered stencil at the boundary point for discretizing the boundary condition equation, (b) Centered stencil at the boundary point for discretizing the Laplace equation, (c) Actual stencil used for the numerical treatment at the boundary point. The solid point is the point of interest and the hollow points constitute the computational stencil. The hollow points highlighted with dashed surrounding lines denote the ghost points. The black thick line represents the boundary

mented in the open source OceanWave3D[26] is adopted. This numerical model is capable of describing the development and propagation of fully nonlinear three-dimensional waves up to the breaking. It has been validated in terms of grid convergence for both two- and three-dimensional problems and the computational effort is shown to scale as the number of grid points.

For three-dimensional inviscid, incompressible and irrotational flows, the flow variables, i.e., velocity potential $\varphi(x, y, z, t)$, free surface evolution $\eta(x,$

$y, t)$, are related by Eqs. (1)-(5) in Cartesian coordinates. The Cartesian coordinate system is arranged such that the xy plane lies on the still water level with the z axis pointing upwards, and the positive x axis corresponds to the wave propagation direction. Eqs. (1)-(3) include the Laplace equation and the boundary value restrictions at the free surface and the bottom, and Eqs. (4)-(5) represent the kinematic and dynamic free surface conditions, respectively. The separation of the kinematics at the free surface from the main field facilitates the iterative numerical procedure and time marching.

$$\nabla_H{}^2\varphi + \frac{\partial^2\varphi}{\partial z^2} = 0, \quad -h \le z < \eta \tag{1}$$

$$\varphi = \tilde{\varphi}, \quad z = \eta \tag{2}$$

$$\frac{\partial\varphi}{\partial z} + \nabla_H h \cdot \nabla_H \varphi = 0, \quad z = -h \tag{3}$$

$$\frac{\partial\eta}{\partial t} = -\nabla_H\eta \cdot \nabla_H\tilde{\varphi} + \tilde{w}(1 + \nabla_H\eta \cdot \nabla_H\eta) \tag{4}$$

$$\frac{\partial\tilde{\varphi}}{\partial t} = -g\eta - \frac{1}{2}[\nabla_H\tilde{\varphi} \cdot \nabla_H\tilde{\varphi} - \tilde{w}^2(1 + \nabla_H\eta \cdot \nabla_H\eta)] \tag{5}$$

where the symbol $\nabla_H = (\partial/\partial x, \partial/\partial y)$ denotes the gradient in the horizontal plane, $\tilde{\varphi}$ and $\tilde{w}$ are the velocity potential and vertical velocity at the free surface respectively.

To treat the time-dependent free surface forming a priori unknown boundary on top of the computational domain, the flow variables are modified vertically and mapped to a time-invariant cuboid domain using the non-conformal σ-coordinate transformation Eq. (6). In the transformed (x, y, σ) domain, Eqs. (1)-(3) become Eqs. (7)-(9) with $\varphi(x, y, z, t)$ replaced by $\Phi(x, y, \sigma, t)$. Eqs. (7)-(9), (4), (5) thus constitute the closed model for the fully nonlinear potential flow, and are treated with the classic fourth-order Runge-Kutta (RK) scheme[26].

$$\sigma = \frac{z + h(x, y)}{\eta(x, y, t) + h(x, y)} \tag{6}$$

$$\nabla_H{}^2\Phi + \frac{\partial\Phi}{\partial\sigma}\nabla_H{}^2\sigma + 2\nabla_H\sigma \cdot \nabla_H\left(\frac{\partial\Phi}{\partial\sigma}\right) +$$

$$\left[\nabla_H\sigma \cdot \nabla_H\sigma + \left(\frac{\partial\sigma}{\partial z}\right)^2\right]\frac{\partial^2\Phi}{\partial\sigma^2} = 0,$$

$$0 \le \sigma < 1 \tag{7}$$

$$\Phi = \tilde{\varphi}, \quad \sigma = 1 \tag{8}$$

$$\left(\frac{\partial\sigma}{\partial z} + \nabla_H h \cdot \nabla_H\sigma\right)\frac{\partial\Phi}{\partial\sigma} + \nabla_H h \cdot \nabla_H\Phi = 0, \quad \sigma = 0 \tag{9}$$

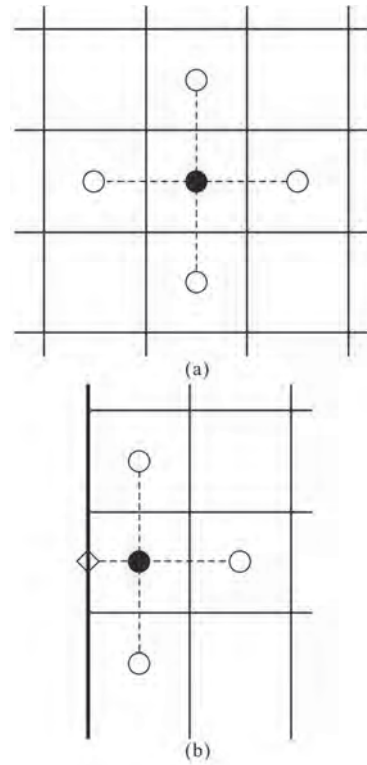where $h(x, y)$ is the still water depth.

Fig. 3 Two-dimensional FVM discretization for internal and boundary cells: (a) Centered stencil at the internal cell, (b) Pseudo centered stencil at the boundary cell. The solid point is the cell center of interest and the hollow points constitute the computational stencil. The black thick line represents the boundary

Equations (7)-(9) are solved by a flexible order finite difference method (FDM) in OceanWave3D. During the FDM operation, for internal points in the computational domain, the Laplace equation (7) is discretized and solved, and a centered stencil where the numbers of points in the positive and negative coordinate directions from the point of interest are identical is used in calculating the derivatives (see Fig. 1(a)). Note that the inclusion of the four corner points in the stencil in Fig. 1(a) is due to the cross-derivative terms in the Laplace equation (7) in the transformed (x, y, σ) domain. For points at boundaries, the computational stencil becomes off-centered (see Fig. 1(b)) and the boundary condition equation rather than the Laplace equation is solved. This numerical treatment for the boundary points is prone to induce

numerical instabilities[29]. In Engsig-Karup et al.[26], a different approach is applied at boundaries. In order to implement the Laplace equation at boundaries, a layer of ghost points surrounding the computational domain is introduced. With the extra points, a centered stencil for the numerical discretization of the Laplace equation is formed as shown in Fig. 2(b). The flow variables at the ghost points out of the domain can be obtained through the boundary condition equation using a stencil similar to that shown in Fig. 2(a). Ultimately, the computational stencil used for the numerical treatment of boundary points looks like that in Fig. 2(c). This numerical scheme for the boundary points can be seen as the Laplace equation with the boundary condition built in, and contributes to maintain a diagonally dominant algebraic equation matrix even in the limit of a linear problem on a constant depth[26].

1.2 Viscous flow model

In the domain decomposition approach, the viscous flow model is used where the inviscid and irrotational flow assumption is violated, e.g., wave breaking and vortex shedding region near structures. The coupling interface between the potential and viscous flow models should be placed sufficiently upstream of these strongly nonlinear flow regions in order to fully exploit the viscous flow model. In the present paper, the multiphase viscous flow model implemented in the open source OpenFOAM-v2012 is used.

$$\nabla \cdot \boldsymbol{u} = 0 \tag{10}$$

$$\frac{\partial \rho \boldsymbol{u}}{\partial t} + \nabla \cdot (\rho \boldsymbol{u}\boldsymbol{u}) = -\nabla p_d - \boldsymbol{g} \cdot \boldsymbol{x} \nabla \rho +$$

$$\nabla \cdot [\mu(\nabla \boldsymbol{u} + (\nabla \boldsymbol{u})^{\mathrm{T}})] + \sigma \kappa \nabla \alpha \tag{11}$$

where the symbols $\boldsymbol{u}$ and p denote the velocity vector and pressure of the flow, respectively. A dynamic pressure p_d defined as $p_d = p - \rho \boldsymbol{g} \cdot \boldsymbol{x}$ is used in the momentum equation (11) in order to simplify the definition of pressure condition at wall boundaries where the normal gradient of pressure for the air and water phases may be different due to the hydrostatic effect[30]. The pressure gradient due to the surface tension at the air-water interface is accounted for by the fourth term on the right-hand side of Eq. (11).

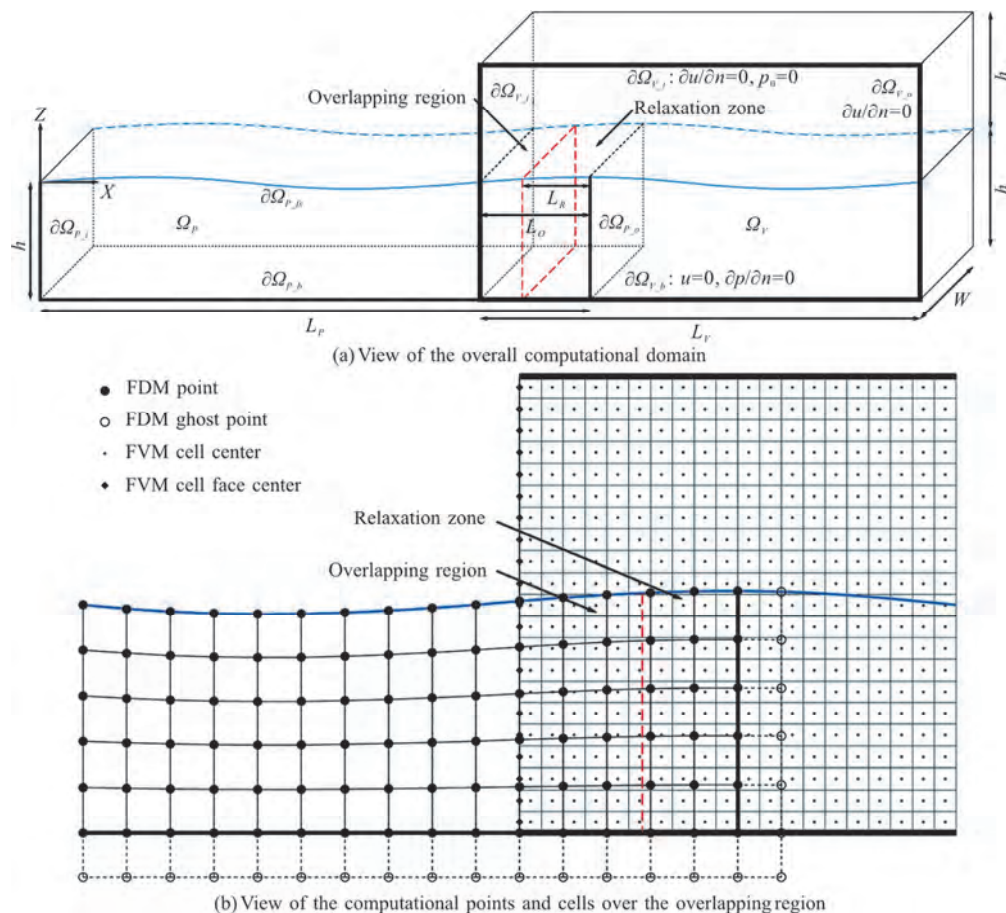The water surface evolution is captured with the VOF model. The surface capturing in VOF is realized

Fig. 4 (Color online) Sketch of the overlapping two-way coupling strategy between OceanWave3D, OpenFOAM

through the volume fraction α which varies from 0 to 1 according to the percentage of one fluid in the cell volume. A water cell is marked by $\alpha = 1$, an air cell is marked by $\alpha = 0$, and the air-water interface is presented where $0 < \alpha < 1$. The advection equation of the volume fraction is given as

$$\frac{\partial \alpha}{\partial t} + \nabla \cdot (\boldsymbol{u}\alpha) + \nabla \cdot [\boldsymbol{u}_r \alpha(1-\alpha)] = 0 \tag{12}$$

where the third term on the left-hand side is an artificial compression contributing to a sharp interface resolution[30]. The symbol $\boldsymbol{u}_r$ defined as the relative velocity between water and air is designated as the compression velocity. In order that the compression acts only in the direction perpendicular to the water surface, the compression velocity is a function of the gradient of volume fraction. With the introduction of volume fraction, the fluid properties at an arbitrary cell are evaluated by weighted average, e.g., $\rho = \alpha\rho_{\text{water}} + (1-\alpha)\rho_{\text{air}}$.

Equations (12), (10) and (11) are solved in sequence during the numerical time stepping using the finite volume method (FVM) in OpenFOAM. A collocated grid distribution is utilized with the flow variables stored at cell centers. The FVM discretization operates in analogy to FDM for internal cells where a centered stencil is used as shown in Fig. 3(a). For boundary cells, a pseudo centered stencil is applied, in which the face center is used instead of the cell center at the boundary side for imposing the boundary conditions (see Fig. 3(b)). Thus, either Dirichlet or Neumann type boundary condition can be easily incorporated during the FVM discretization at boundary cells. However, for coupling the viscous flow model with a potential flow model, the interface boundary should assume the role to both transfer and convert data, thus bringing difficulties of the boundary condition definition. The difficulties arise from the incompatibility of equations and primitive flow variables between the potential and viscous flow models as presented above, as well as the numerical methods.
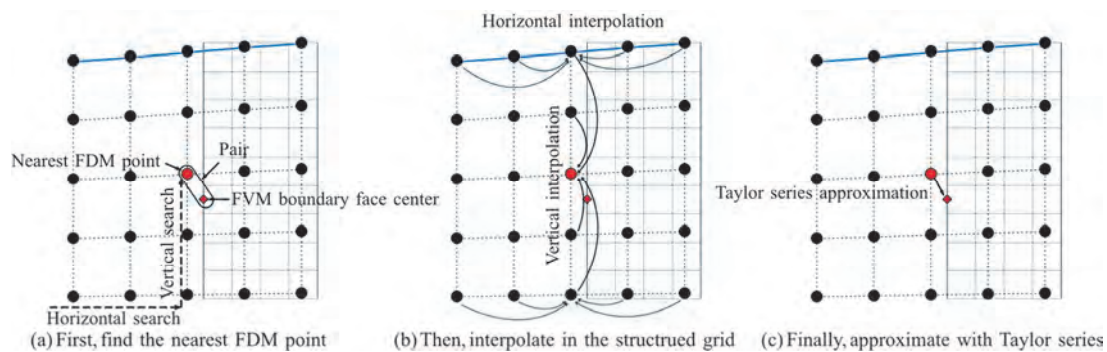

Fig. 5 (Color online) Illustration of the procedure for grabbing the target data in OceanWave3D
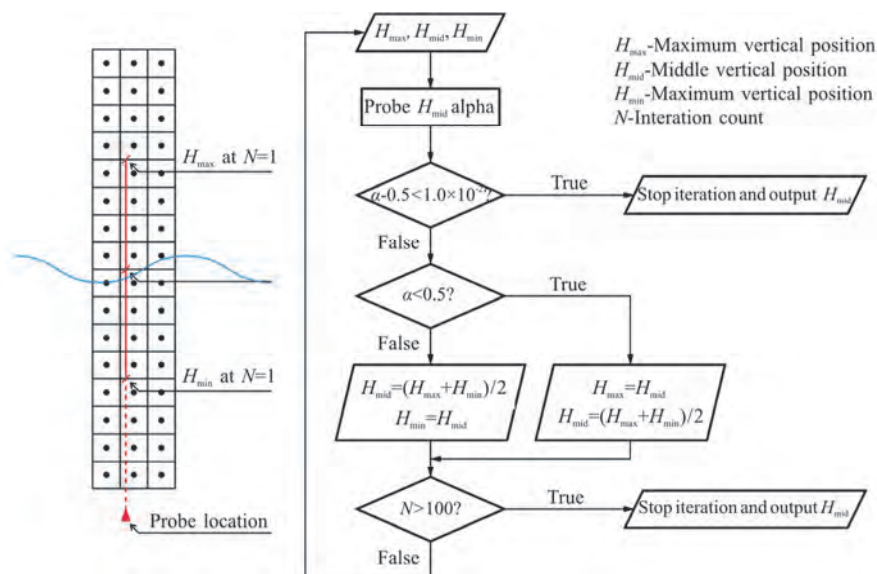

Fig. 6 (Color online) Sketch of the iterative algorithm for locating the free surface

In particular, for the present research, the mismatch between FDM points in OceanWave3D, FVM cells in OpenFOAM requires point-to-cell and cell-to-point interpolation during the data sampling. The concept and details of the two-way coupling strategy are described in Section 3.

2. Two-way coupling strategy on the potential and viscous flow models

2.1 Concept

For coupling the potential and viscous flow models, two strategies are usually applied. The first strategy is featured by an overlapping between the two model domains[19-20]. The overlapping region facilitates the two confining lateral boundaries which correspond to the inlet or outlet of the two model domains to construct updated boundary conditions through probing data in the internal field of the coupled models. This strategy may be flawed due to the increase in domain length and the addition of numerical parameters, i.e., the position and width of the overlapping region. The second strategy maintains a concise domain without overlapping[17-18]. In order that the conditions on the two sides of the single matching boundary advance in time alternately, the unsteady Bernoulli equation is used in the potential flow model to construct the Dirichlet boundary condition. Compared to the strategy with overlapping, the strategy without overlapping possesses a greater efficiency but appears less robust[19]. This aspect makes the non-overlapping strategy a secondary choice for consideration.

In the present research, the overlapping strategy is employed for coupling the potential flow model OceanWave3D, the viscous flow model OpenFOAM.

The coupling procedure is straightforward in terms of transferring water surface elevation and velocity data between the flow models while the ghost point approach in OceanWave3D is utilized and a relaxation zone is built near the outlet in the OceanWave3D domain for consideration of computational stability. The strategy is illustrated in Fig. 4.

2.2 Spatial coupling

As shown in Fig. 4(a), the computational domain consists of the upstream OceanWave3D domain Ω_P, the downstream OpenFOAM domain Ω_V such that waves are generated at the inlet $\partial\Omega_{P\_i}$ in the potential flow model, and highly nonlinear waves which occur downstream are captured by the viscous flow model and absorbed at the outlet $\partial\Omega_{P\_o}$ in an active manner. For details on the active wave absorption, see Higuera et al.[3]. The incident and reflected wave propagations between the OceanWave3D, OpenFOAM domains are realized through the two-way coupling across the mutual flow region delimited by $\partial\Omega_{P\_o}$, $\partial\Omega_{P\_i}$. The bottom boundaries $\partial\Omega_{P\_b}$, $\partial\Omega_{V\_b}$ in respective domains are smoothly connected while the free surface $\partial\Omega_{P\_fs}$ in OceanWave3D is associated with the VOF captured water surface in OpenFOAM. The top boundary $\partial\Omega_{V\_t}$ in the OpenFOAM domain serves as connecting it to the atmosphere.

The data transfer during the two-way coupling occurs across $\partial\Omega_{P\_o}$, $\partial\Omega_{V\_i}$, near which the distributions of FDM points, FVM cells are plotted in Fig. 4(b). The grid size in OceanWave3D is assumed to be larger than that in OpenFOAM. In the case when
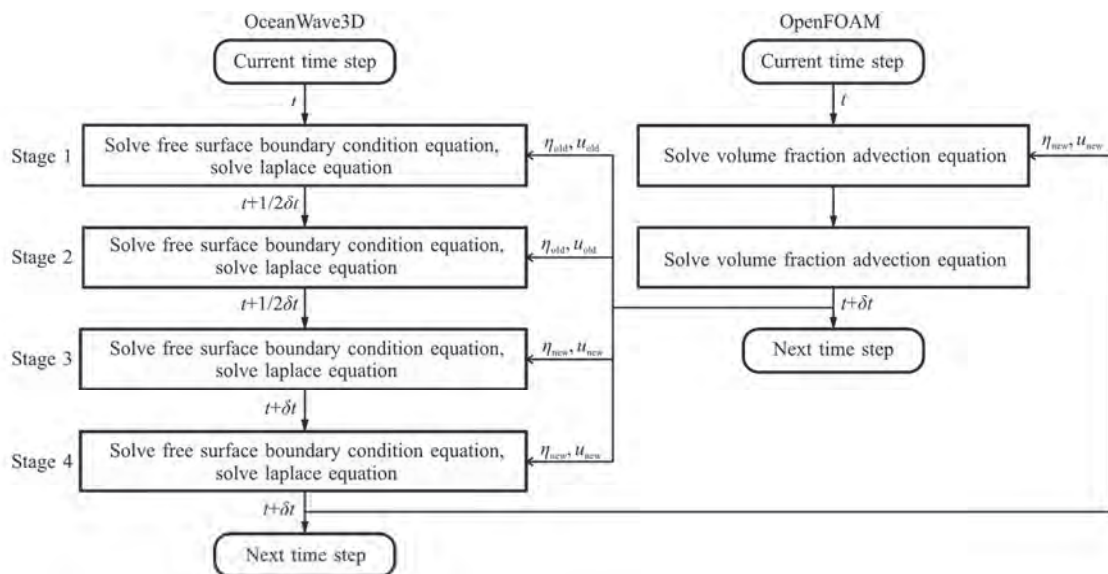

Fig. 7 Algorithm of the two-way coupling between OceanWave3D, OpenFOAM

incident waves propagate from Ω_P to Ω_V, the free surface elevation and velocity at the FDM points near $\partial\Omega_{V\_i}$ calculated in OceanWave3D are used to obtain the corresponding values at the FVM cell face centers along $\partial\Omega_{V\_i}$ activating the OpenFOAM computation. The transfer of data posts no difficulty as the free surface elevation is simply interpolated and the velocity is the spatial derivative of the velocity potential in the three coordinate directions. The interpolation employs a Taylor series approach (see Eq. (13)), in which the nearest FDM point to each FVM boundary face center is searched to be used as the central position based on the structured grid. Figure 5 illustrates the calculation procedure for grabbing the target surface elevation and velocity in OceanWave3D. Note that for surface elevation, only horizontal interpolation is needed in the second step.

$$\Psi(\boldsymbol{x}+\delta\boldsymbol{x}) = \sum_{n=0}^{2a} \frac{\delta x_i^n}{n!} \frac{\partial^n \Psi}{\partial x_i^n}(\boldsymbol{x}) \tag{13}$$

where Ψ refers to surface elevation or velocity components, n is a user specified order parameter and the computational stencil coefficients for the consecutive orders of partial differential derivatives are calculated using a weight subroutine.

The reflected wave propagation from Ω_V to Ω_P is accomplished using the ghost point approach in OceanWave3D. In OceanWave3D computations, the ghost points serving as one wing of the computational stencil for the boundary points are evaluated based on the boundary conditions. It is important to note that in contrast to the ghost points at the bottom, during the algebraic equation matrix construction step, the derivative of velocity potential other than the velocity potential is calculated at the ghost points of lateral boundaries, which is forced to equal any input velocity value. This may be a preferable implementation for introducing flow fluxes into the OceanWave3D computation. Utilizing this feature, for the present two-way coupling, the calculated results at the ghost points adjacent to $\partial\Omega_{P\_o}$ are forced to equal the velocity at the FDM points along $\partial\Omega_{P\_o}$ with the value probed in the OpenFOAM domain. Besides, a crucial aspect for the OceanWave3D computation is the wave absorption at outlet. To mirror the outlet damping in the two-way coupling realization, the displacement and velocity potential at the free surface over the overlapping region are relaxed using the sampled values from OpenFOAM, thus forming a relaxation zone near the outlet of the OceanWave3D
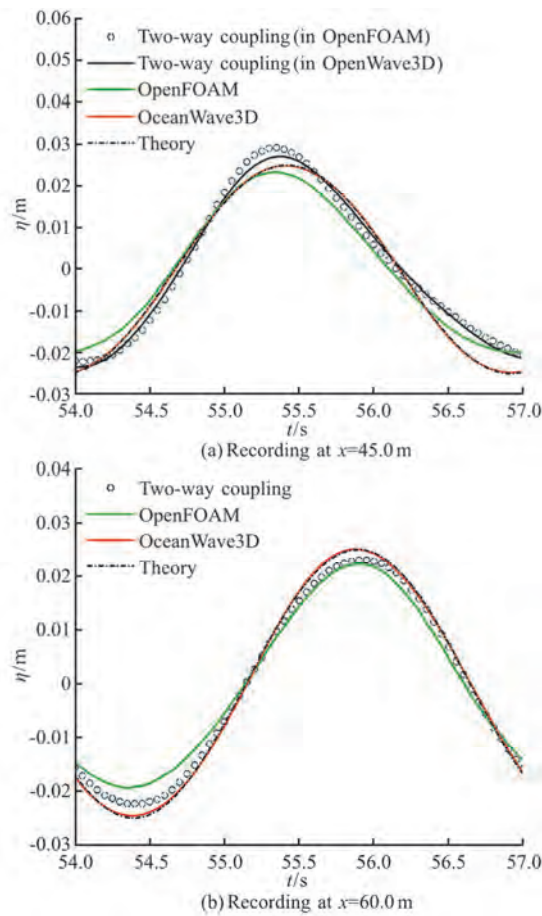
Table 1 Parameters of the waves

Wave type	Spectrum	Height, H	Depth, h	Period, T
Stokes I	-	0.05 m	0.6 m	3.0 s
Stokes II	-	0.05 m	0.4 m	3.0 s
Irregular	JONSWAP	4.00 m	50.0 m	9.0 s
Multi-directional irregular	JONSWAP, normal spreading	2.00 m	80.0 m	8.0 s

Table 2 Parameters of the computational domain for Stokes I wave case

Test	L_P	L_V	L_O	L_R	L_S	L_W	W	h	h_a
Positive propagation	50 m	30 m	10 m	2.5 m	-	-	-	0.6 m	0.2 m
Negative propagation	50 m	30 m	10 m	2.5 m	-	-	-	0.6 m	0.2 m
Impact on wall	50 m	30 m	10 m	2.5 m	60 m	0.4 m	-	0.6 m	0.2 m

Table 3 Parameters of the computational domain for Stokes II wave case

Test	L_P	L_V	L_O	L_R	L_S	L_W	W	h	h_a
Positive propagation	50 m	30 m	10 m	2.5 m	-	-	-	0.4 m	0.2 m
Negative propagation	50 m	30 m	10 m	2.5 m	-	-	-	0.4 m	0.2 m
Impact on wall	50 m	30 m	10 m	2.5 m	60 m	0.4 m	-	0.4 m	0.2 m

Table 4 Parameters of the computational domain for irregular wave case

Test	L_P	L_V	L_O	L_R	L_S	L_W	W	h	h_a
Positive propagation	500 m	400 m	100 m	50 m	-	-	-	50 m	25 m
Negative propagation	500 m	400 m	100 m	50 m	-	-	-	50 m	25 m
Impact on wall	500 m	400 m	100 m	75 m	600 m	4 m	-	50 m	25 m
Impact on square (3-D)	500 m	400 m	100 m	50 m	600 m	4 m	20 m	50 m	25 m

Table 5 Parameters of the computational domain for multi-directional irregular wave case

Test	L_P	L_V	L_O	L_R	L_S	L_W	W	h	h_a
Positive propagation	400 m	300 m	100 m	50 m	-	-	100 m	80 m	20 m

Fig. 8 (Color online) Free surface displacement for the Stokes I wave positive propagation case

Fig. 9 (Color online) Free surface displacement for the Stokes I wave negative propagation case

domain (see Fig. 4(a)). The width of the relaxation zone is deliberately set to be smaller than that of the overlapping region in order to maintain a clearance between forward and backward data transfers. The relaxation approach expressed by Eqs. (14), (15) is used. Note that the relaxation factor calculated by the polynomial scheme (15) exhibits a smooth transition to both limits and is found to be a stable choice in comparison to the sponge-like and exponential schemes.

$$\phi = (1 - \lambda)\phi_{\text{OceanWave3D}} + \lambda\phi_{\text{OpenFOAM}} \qquad (14)$$

$$\lambda = 1 - (3.0 \times x^3 - 2.0 \times x^2) \qquad (15)$$

where x represents the dimensionless distance to the outlet with respect to the relaxation zone width and retains the λ values of 0, 1 at the left and right ends of the zone respectively.

During the reverse data transmission, both the surface elevation and velocity potential at the water surface need to obtained from OpenFOAM. Figure 6 illustrates the iterative algorithm for identifying the free surface location with the VOF model. It includes
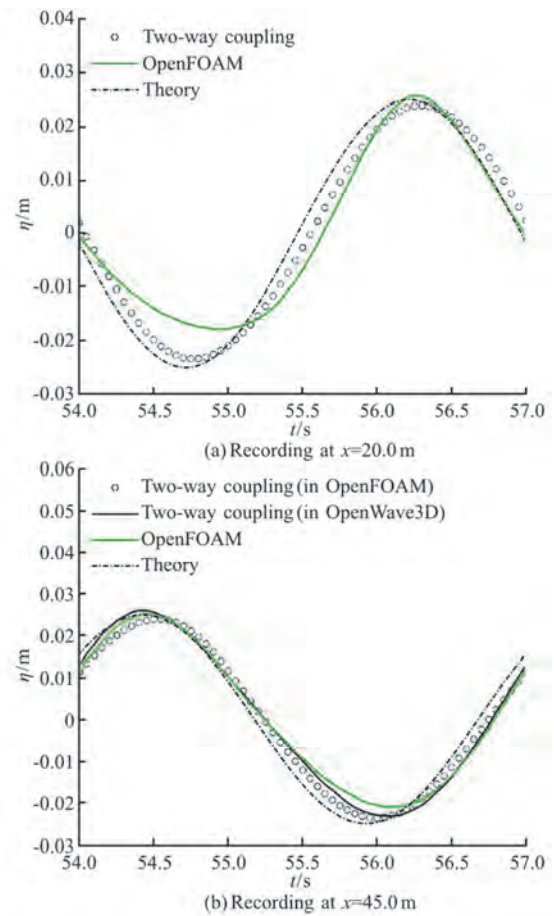
horizontal search to reduce the candidate cells array and then vertical search to iteratively locate the free surface. At each horizontal probe location, a limit of one hundred iterations is prescribed in the vertical search, and the loop exists either when the required loop number is fulfilled or when the pre-defined difference in α value to 0.5 is met. While the surface elevation can be directly probed, there is no easy way to obtain the velocity potential in the viscous flow model. For the velocity potential data, a trick is applied herein to reduce the complexity of the problem. Recall that in OceanWave3D computations, Eqs. (4), (5) and (7)-(9) are solved alternately:

(1) The vertical velocity at the free surface, together with the spatial derivatives of the free surface displacement and velocity potential, is used in the right-hand side of Eqs. (4), (5). The resultant left-hand side of Eqs. (4), (5), i.e., the temporal derivatives of the free surface displacement and velocity potential, is then used to advance the corresponding variables in time. The updated free surface displacement and velocity potential are used as the boundary conditions during the new time step.
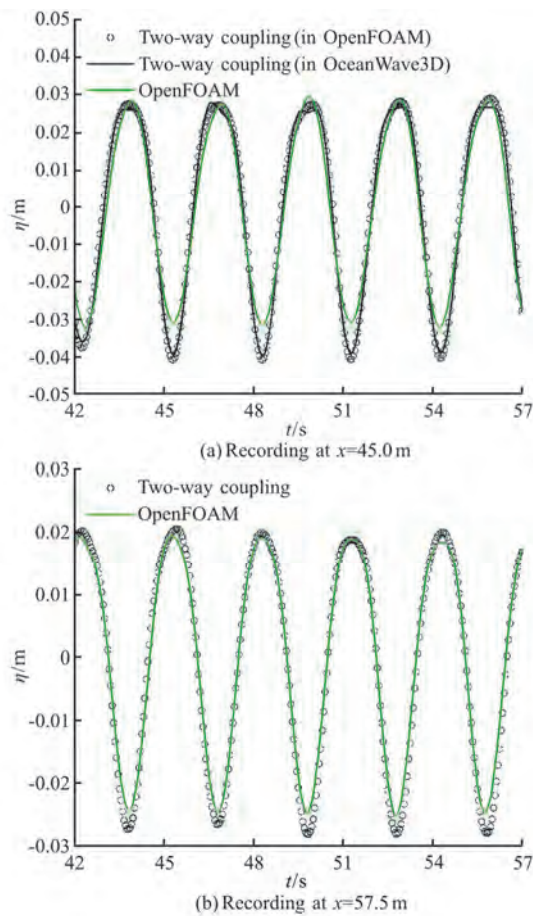
Fig. 10 (Color online) Free surface displacement for the Stokes I wave impacting on a wall case

Fig. 11 Free surface profiles in the OceanWave3D subdomain for the Stokes I wave impacting on a wall case

(2) Eqs. (7)-(9) are solved under the new free surface boundary conditions, and the vertical velocity at the free surface is calculated and is then used in the next time step calculation.

In the two-way coupling procedure, the updated free surface displacement at the end of phase 1 is kept consistent with OpenFOAM, and the sampled velocity from OpenFOAM is used in calculating the temporal derivative of velocity potential for updating the velocity potential. Notice that the terms in the right-hand side of Eq. (5) are composed of either velocity or the spatial derivative of velocity potential which is velocity in nature, and this is the reason that the trick arises. The idea is that if the time variation of velocity potential is set correctly, the updated velocity potential should be correct accordingly.

2.3 Temporal coupling

The temporal coupling between OceanWave3D and OpenFOAM realizes in a staggered manner, meaning that the two flow models advance in time alternately, while different time stepping methods are used in respective models. The two-way coupling algorithm is illustrated in Fig. 7. In OceanWave3D,
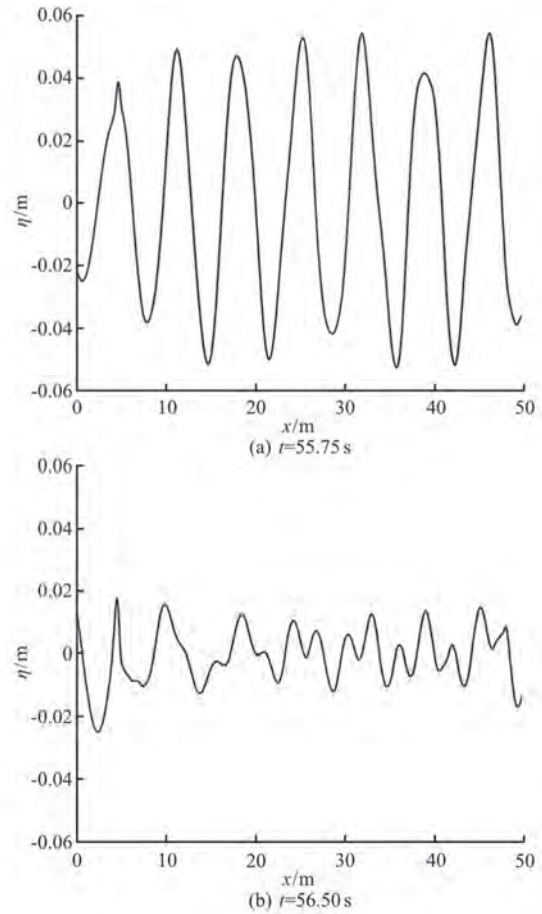
the classic fourth-order RK scheme is used at each time step. At each stage of the RK procedure, the free surface elevation and velocity at the outlet relaxation zone are modified according to OpenFOAM. This is regarded as a strong imposition of the reflected wave response as compared to a weak manner, in which only the first RK stage participates in the data reception, and the strong imposition is found to be a necessity for severe wave reflections. The free surface and velocity are then updated through the four stages of the RK procedure, and are transferred back to OpenFOAM. In OpenFOAM, field operation and manipulation are proceeded under the newly updated inlet patch value. Note that the PIMPLE algorithm is used to treat the pressure velocity coupling issue in OpenFOAM, and a description of the PIMPLE algorithm is referred to Zhong et al.[31-32].

3. Validation test results and discussion

3.1 Numerical settings

Linear, nonlinear, irregular, and multi-directional irregular waves are used to validate the two-way
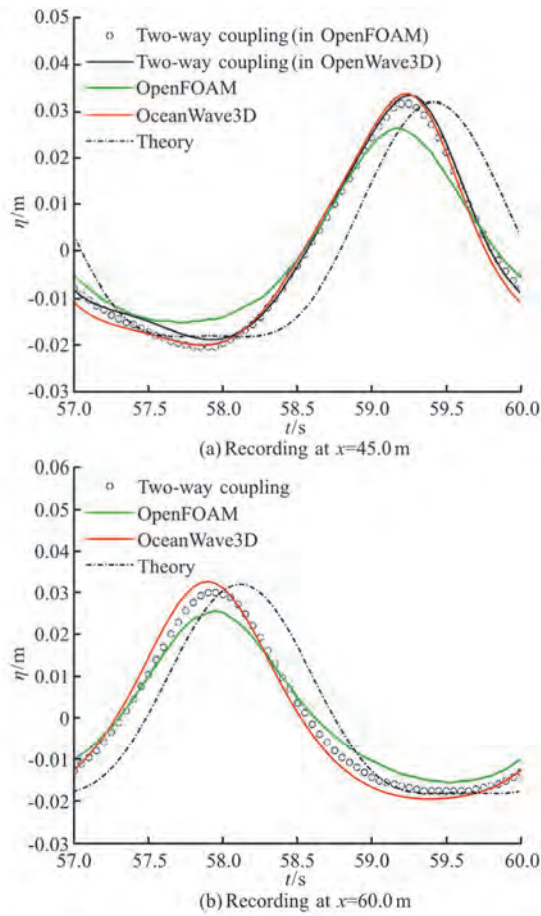
Fig. 12 (Color online) Free surface displacement for the Stokes II wave positive propagation case

Fig. 13 (Color online) Free surface displacement for the Stokes II wave negative propagation case

coupling model in two- and three-dimensional situations. For the first three wave cases, three categories of tests are conducted including wave propagation in the positive and negative directions and wave impacting on a wall. The negative wave propagation and wave interacting with a stationary wall are tested such that the effectiveness of the bidirectional coupling is evaluated. For the multi-directional irregular wave, only positive wave propagation is considered to extend the coupling model in three dimensions. The computational domain has a similar layout as that in Fig. 4(a) except that a wall is established in the OpenFOAM domain for the wave structure interaction tests. As shown in Fig. 4(a), the coordinate system is fixed at the still water surface with the x axis aligned with the wave propagation direction and the z axis pointed upwards. L_P and L_V are the horizontal lengths of the OceanWave3D and OpenFOAM domains, respectively. L_O and L_R refer to the widths of the overlapping region and relaxation zone, respectively. Only water phase with a still water depth of h is considered in the OceanWave3D domain while the
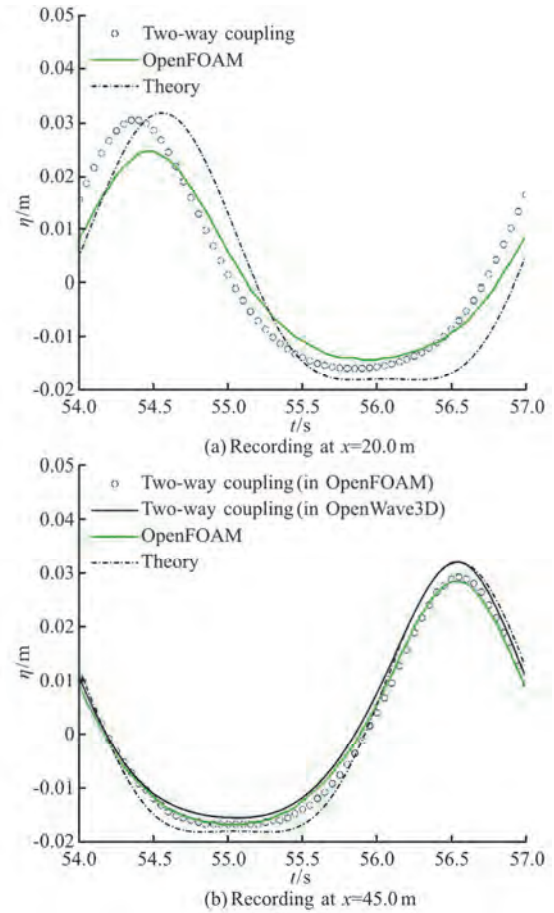
OpenFOAM domain is composed of water at the bottom and air on the top with the atmosphere boundary set h_a above the still water level. The wall with a width of L_W is positioned in the middle of the horizontal span of the OpenFOAM domain with a total distance of L_S to the inlet $\partial \Omega_{P\_i}$. The parameters of the waves are given in Table 1, and the parameters of the computational domain for the two-way coupling simulations are presented in Tables 2-5. Note that individual OpenFOAM simulations are also conducted for comparison in the present research, and the total length of the computation domain is simply calculated as $L = L_P + L_V - L_O$. A uniform mesh is generated for the simulations. Mesh convergence study has been performed on OpenFOAM computations. For the two-dimensional cases, three grids with 2.8×10^5, 7.2×10^5 and 1.1×10^6 cells are used. Results show that the three mesh densities can give similar results and thus the medium mesh is used in all the simulations. For the three-dimensional cases, converged meshes have been used which result in
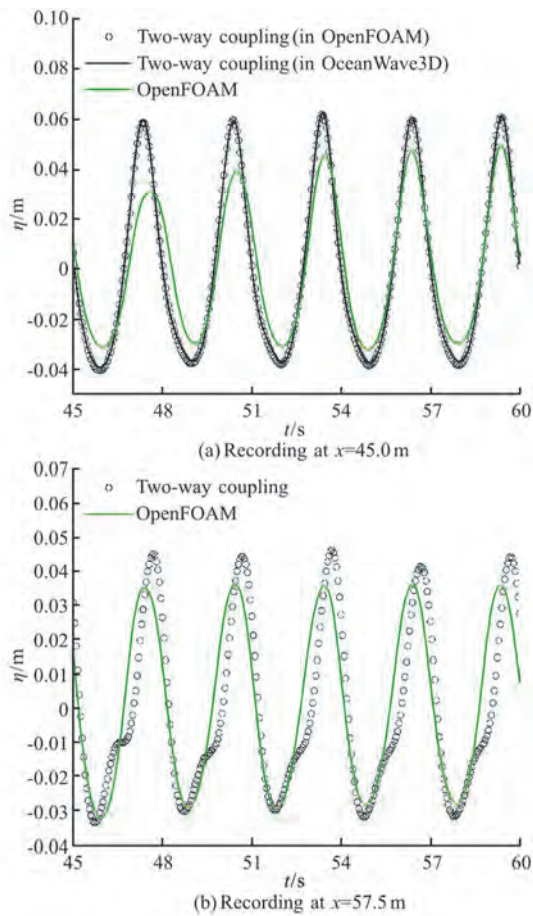
Fig. 14 (Color online) Free surface displacement for the Stokes II wave impacting on a wall case

Fig. 15 Free surface profiles in the OceanWave3D subdomain for the Stokes II wave impacting on a wall case

2.4×10^6, 3.0×10^6 cells for irregular and multi-directional irregular waves in OpenFOAM simulations respectively.

3.2 *Stokes I wave*

Figures 8-10 are the surface elevation history for the positive and negative propagations and impacting on a wall of Stokes I wave. Individual OpenFOAM simulations are also performed for comparison. The theoretical solution given by Eq. (16) is added in Figs. 8, 9, and the minus sign in the phase term should be changed to plus sign for negative propagation case.

$$\eta = \frac{H}{2}\cos(kx - \sigma t) \qquad (16)$$

It is seen in Fig. 8 that at both recording locations, the potential flow model OceanWave3D results match perfectly with the theoretical value while the coupling simulation deviates slightly from theory. The deviation is notably larger for the OpenFOAM results as shown in Figs. 8(a), 8(b). This is regarded by the authors to be associated with the numerical dissipa-
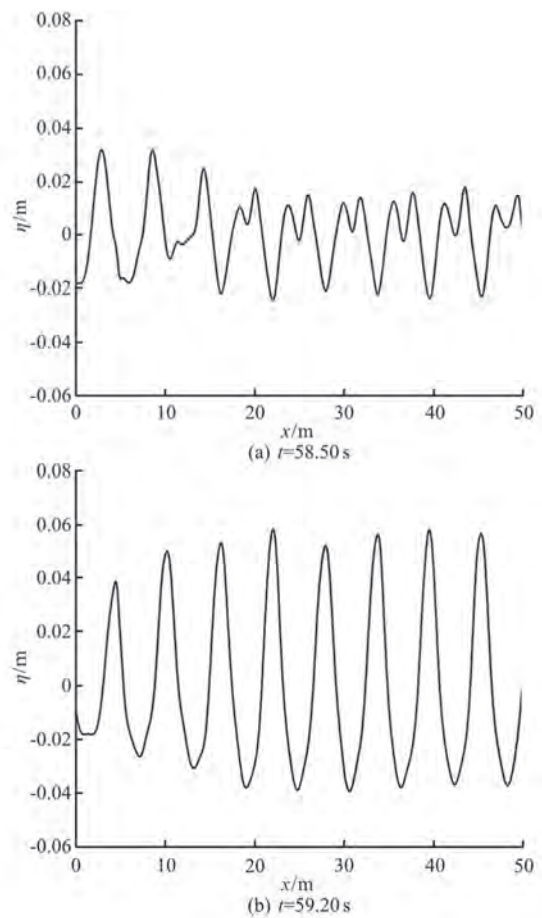
tions in the viscous flow model. Thus, it is likely that the slight deviation in the coupling simulation relates to the numerical errors in the viscous flow model provided that the effectiveness of information share during the two-way coupling is manifested in Fig. 8(a) where the surface elevation in the overlapping region agrees well between two subdomains. To state it more clearly, since the free surface displays a smooth transition between the coupled models, the data must be smoothly imposed in the bidirectional coupling especially for the reverse transfer otherwise the surface near the outlet of the OceanWave3D domain would rise unlimitedly leading to computational divergence. A direct case to show the reverse data transfer is the negative wave propagation in Fig. 9. For the negative propagation test, the location $x = 20.0\,\text{m}$ is upstream of the location $x = 45.0\,\text{m}$, and the inlet and outlet boundary conditions of the OpenFOAM domain in Fig. 4(a) are exchanged such that the OpenFOAM outlet assumes the role to both actively absorb the wave and bidirectionally couple with OceanWave3D. It is seen in Fig. 9 that good agreement between the coupling simulation and target
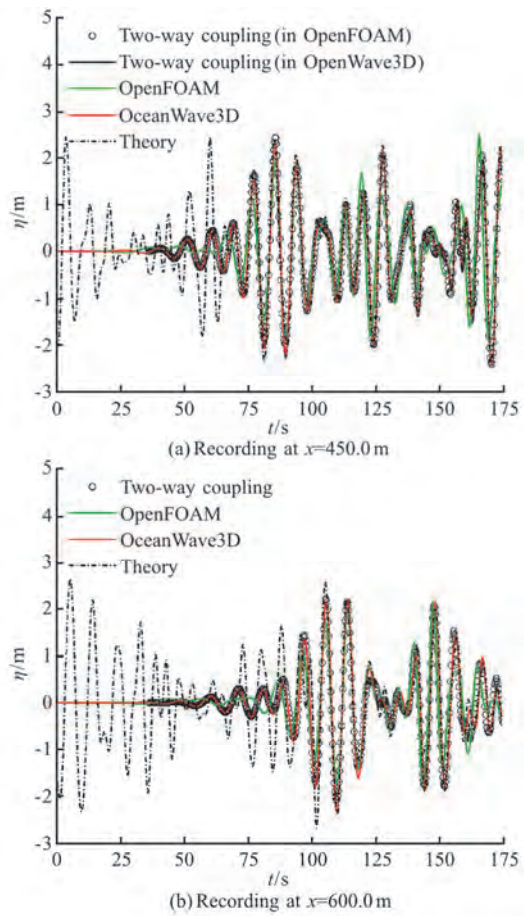
Fig. 16 (Color online) Free surface displacement for the irregular wave positive propagation case

Fig. 17 (Color online) Free surface displacement for the irregular wave negative propagation case

results is obtained while OpenFOAM underrates the wave amplitude especially in the downstream where higher numerical dissipation is accumulated. The effective data transmission in the two-way coupling is registered in two ways. One is the perfect match in surface elevation between two subdomains in Fig. 9(b), and the other is the agreement of the surface displacement to the theoretical target in the potential flow subdomain (see Fig. 9(a)) where the free surface is thoroughly aroused by the data transmission across the relaxation zone. The negative wave propagation can be seen as an extreme case which is merely used for validation in the present research as the potential flow model is usually arranged upstream of the viscous flow model. The wave impacting on a wall is another extreme case as the incident and completely reflected waves interact over the overlapping region putting the two-way coupling to the test. Figure 10 shows that underprediction in surface evolution is present by the OpenFOAM simulation though both types of simulations give identical wave form and phase. As no resource other than OpenFOAM results which are tagged with numerical errors is available,
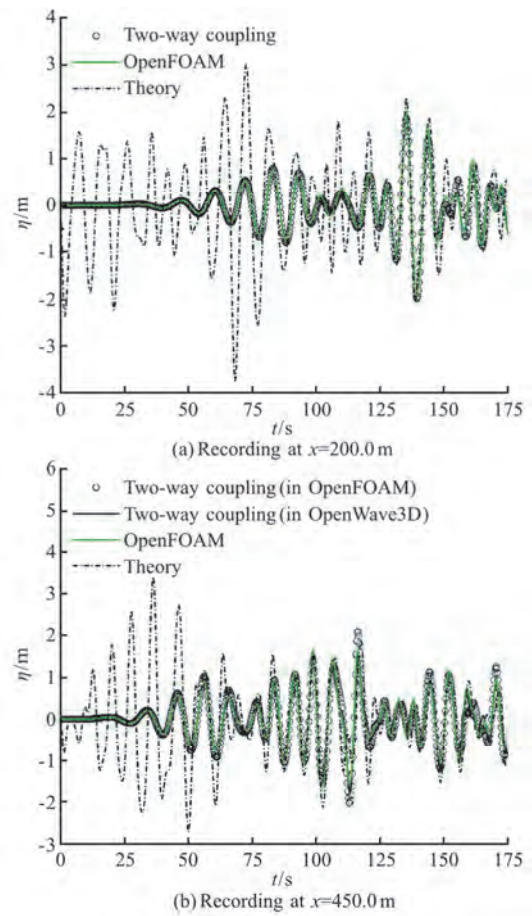
the water surface match in the overlapping region shown in Fig. 10(a) convincingly demonstrates the reliability of the coupling strategy even in the full reflection test. Besides, the surface profiles in the OceanWave3D subdomain at two times are shown in Fig. 11. The two selected times, i.e., $t = 55.75\,\text{s}$, $t = 56.50\,\text{s}$, correspond to the instants when the incident and reflected waves touch and separate respectively. It is demonstrated that the wave interactions undergone in the OpenFOAM subdomain are transferred to the OceanWave3D subdomain via the effective coupling.

3.3 *Stokes II wave*

Figures 12-14 show the results of the three classes of tests for Stokes II wave. The theoretical solution given by Eq. (17) is added in Figs. 12,13, and the minus sign in the phase term should be changed to plus sign for negative propagation case.

$$\eta = \frac{H_1}{2}\cos(kx - \sigma t) +$$

$$\frac{kH_1^2}{16}\frac{\{3.0-[\tanh(kh)]^2\}}{[\tanh(kh)]^3}\cos[2(kx-\sigma t)] \qquad (17)$$
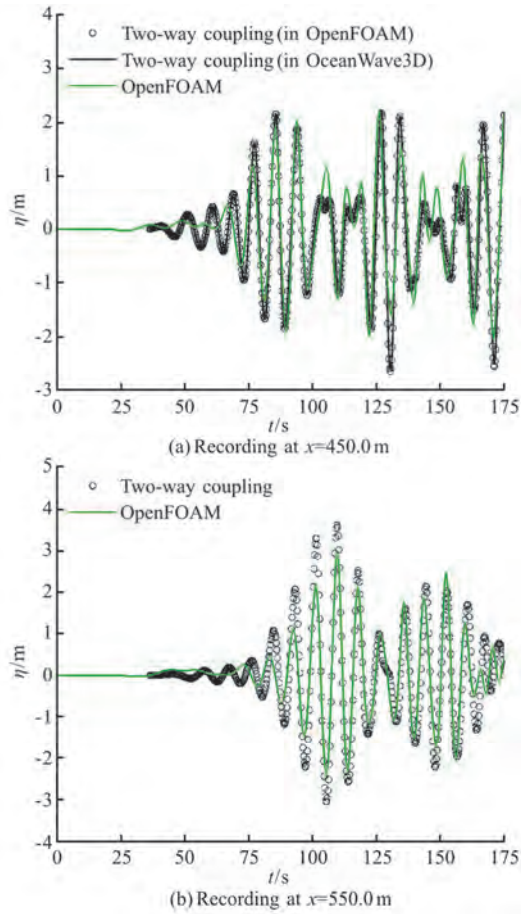

Fig. 18 (Color online) Free surface displacement for the irregular wave impacting on a wall case

Figure 12 shows that there exists a small bump at the trough of the nonlinear wave form, and this featured surface motion is smeared out in both potential and viscous flow models. As seen in the figure, the OceanWave3D and coupling simulations give generally identical results which exhibit some difference to the theoretical value. As the used grid which has around 230 400 cells in two dimensions in OpenFOAM subdomain and a uniform size of 0.0125 m in the horizontal plane is decided by mesh convergence analysis, it is projected that the error is in the sense of numerical implementation which is not the focus of the present research. However, the coupling strategy cannot be undervalued as observed in Fig. 12(a) for the matching imposition in the overlapping region and identical results between potential flow and coupling models. By the way, OpenFOAM results show the most deviation to theory in Fig. 12. For the negative wave propagation case shown in Fig. 13, it is also seen
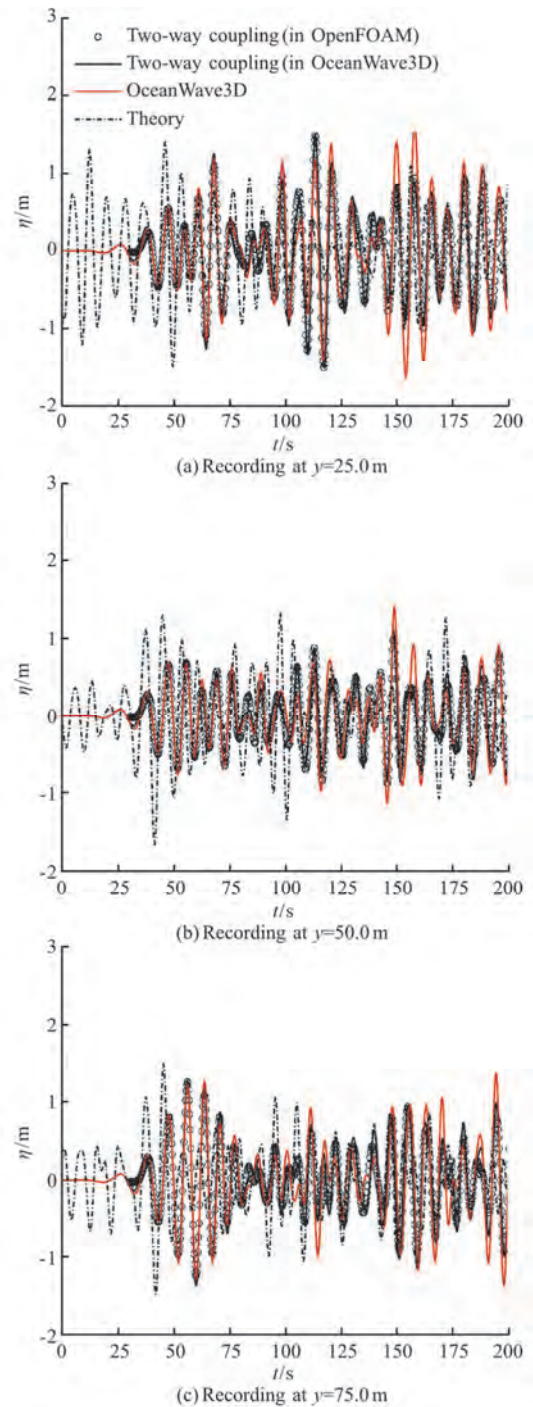
Fig. 19 (Color online) Free surface displacement for the multi-directional irregular wave positive propagation case recorded at $x = 350.0$ m

that the two-way coupling simulation gives a better estimation than OpenFOAM although both results deviate from theory due to numerical errors in treating the plateau at the wave trough. The coupling model is validated to be applicable to nonlinear waves in the sense that the surface elevation across the relaxation
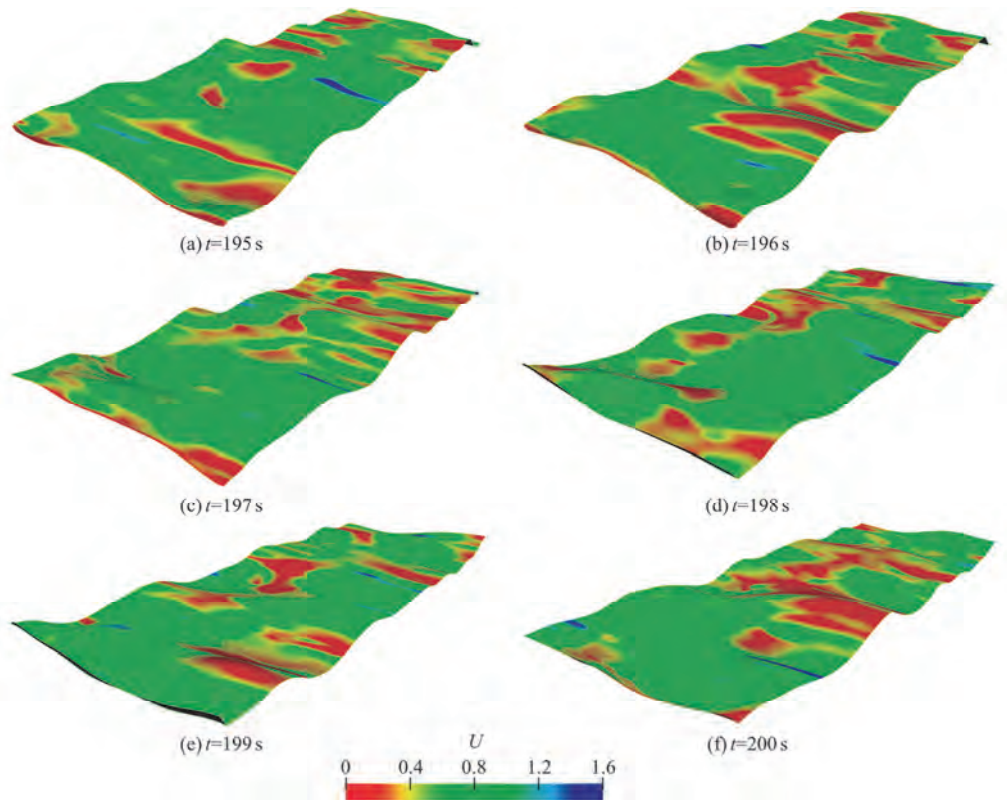
Fig. 20 (Color online) Free surface profiles in the OpenFOAM subdomain for the multi-directional irregular wave propagation case. Note that the vertical coordinate is scaled up by 5 for demonstration purpose

zone is matched in Fig. 13(b), the surface evolution in the downstream potential flow subdomain is induced as anticipated in Fig. 13(a). Since the wave motion in OceanWave3D is directed linked to the flow field near the outlet of the OpenFOAM domain, when the probed value is already contaminated the results downstream would also be affected. For the wave interacting with a wall case, the OpenFOAM simulation notably underpredicts the evolution of the free surface as seen in Fig. 14. The effective two-way coupling is only disclosed via the matched free surface in the overlapping region in Fig. 14(a). Figure 15 illustrates the free surface profiles in the Ocean-Wave3D subdomain at $t = 58.50\,\text{s}$, $t = 59.20\,\text{s}$. It is seen that the wave superposition and separation phenomena proceed throughout the domain maintaining an instantaneous connectivity across the overlapped region.

3.4 Irregular wave

Figutres 16-18 show the validation test results of irregular wave. JONSWAP spectrum is used for the frequency distribution and a random number subroutine is used in generating the irregular initial phase at each frequency. The theoretical solution given by Eq. (18) which combines all frequency components is included in Figs. 16, 17, and the minus sign in the

phase term should be changed to plus sign for negative propagation case.

$$\eta = \sum_{i=1}^{n} \frac{H}{2} \cos(k_i x - \sigma_i t + \varepsilon_i) \tag{18}$$

Figure 16 shows that the coupling model results agree well with the potential flow model and theoretical results after the ramp time in simulations ends while the OpenFOAM results show visible mismatches to target in some time slots. The agreement of surface elevation in the overlapping region shown in Fig. 16(a) further confirms the reliability of the coupling strategy in linking subdomains for severe waves. Note that in the two-way coupling, the viscous flow model is activated only after 36 s when wave moves near to the overlapping region, which helps save a large amount of computing time. The negative wave propagation is also satisfactorily simulated by the two-way coupling model as seen in Fig. 17. Particularly, Fig. 17(b) shows that the free surface is matched between overlapped domains indicating the effective data transfer through the relaxation zone. For the irregular wave reflection by a wall case in Fig. 18, the coupling and OpenFOAM simulations give generally the same wave motion pattern though OpenFOAM slightly underpredicts the surface evolution amplitude.
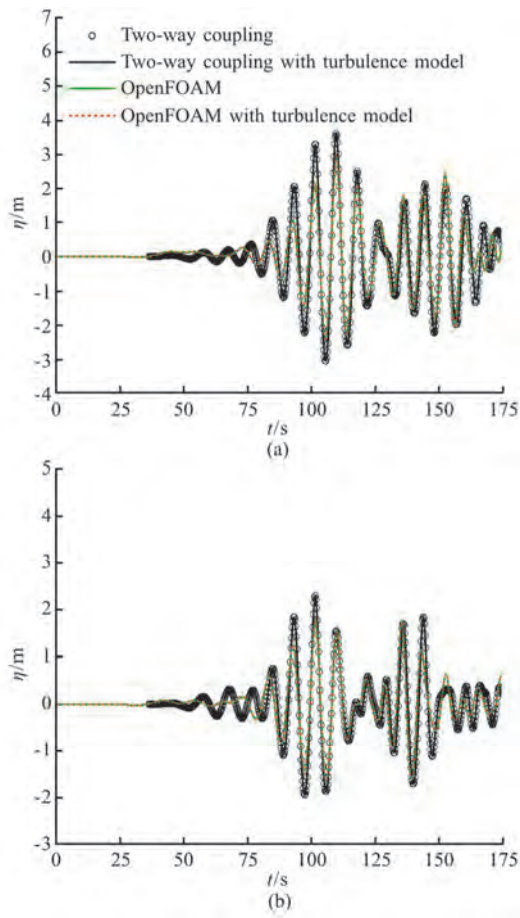
Fig. 21 (Color online) Free surface displacement (a) Recorded at $x = 550.0$ m for the irregular wave impacting on a wall case, (b) Recorded at $x = 550.0$ m, $y = 10.0$ m for the irregular wave impacting on a square cylinder case

It is also seen that the free surface in the overlapping region remains consistent between coupled models throughout the coupling simulation.

3.5 Multi-directional irregular wave

Figure 19 shows the positive propagation test results of multi-directional irregular wave. JONSWAP spectrum combined with a normal spreading is used for the frequency and direction distributions, and initial phases are randomly allocated for each frequency. The theoretical solution given by Eq. (19) which combines all wave components is included in Fig. 19. As the implementation of multi-directional irregular wave in OpenFOAM requires numerous paddles to produce which is tedious and regarded as error prone, pure OpenFOAM simulation is not conducted. The potential flow model and theoretical results are used in the comparison. Note that to save computing time in the three-dimensional simulation, a relatively coarse grid including 1.5×10^6 cells is used in the OpenFOAM subdomain.

$$\eta = \sum_{i=1}^{n} \frac{H}{2} \cos[k_i x \cos(\beta_i) + k_i y \sin(\beta_i) - \sigma_i t + \varepsilon_i]$$

(19)

It is seen in Fig. 19 that in the overlapping region from $x = 300.0$ m to $x = 400.0$ m (see Table 5), the surface elevations at the three gauging points generally agree among the three types of simulations. The deviations in some time slots are presumably attributed to numerical errors associated with the coarse grid as larger deviations are observed at downstream locations. After all, the surface elevations between coupled domains match well in the figures indicating the effectiveness of the coupling model. Figure 20 gives the free surface profiles at six consecutive times to illustrate the aroused wave in the viscous flow domain by the coupling model. Note that the vertical coordinate is scaled up by 5 for demonstration purpose.

3.6 Inclusion of turbulence model

To assess the inclusion of turbulence model in the coupling strategy, RANS with Mentor SST k-ω two equations model is used. The transport principles for the turbulent kinetic energy k, the specific turbulence dissipation ω are given by Eqs. (20), (21). For details of the turbulence model see Zhong et al.[31-32].

Table 6 Comparison of time costs for the validation tests

| Wave type	Test	Type	OpenFOAM	Two-way coupling
Stokes I	Positive propagation	2-D	3.6 h	3.1 h
Stokes I	Impact on wall	2-D	10.1 h	5.6 h
Stokes II	Positive propagation	2-D	2.7 h	2.4 h
Stokes II	Impact on wall	2-D	5.0 h	3.0 h
Irregular	Positive propagation	2-D	9.0 h	4.2 h
Irregular	Impact on wall	2-D	8.2 h	5.9 h
Irregular	Impact on wall (turbulent)	2-D	10.4 h	5.7 h
Irregular	Impact on square	3-D	28.8 h	12.3 h
Irregular	Impact on square (turbulent)	3-D	32.3 h	13.8 h
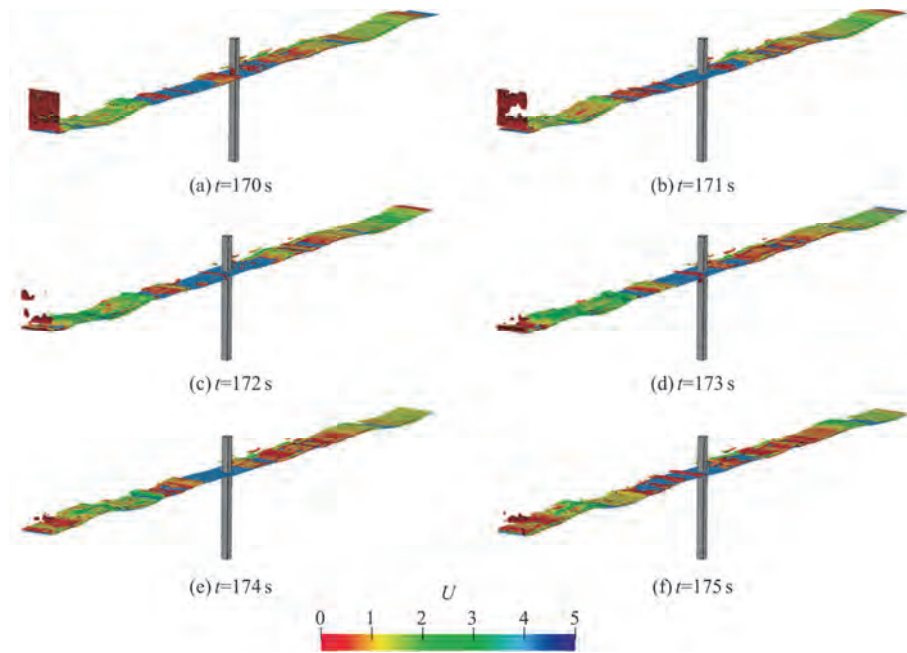
Fig. 22 (Color online) Illustration of y component of vorticity for the irregular wave impacting on a square case. Note that the blue surface represents the air-water interface
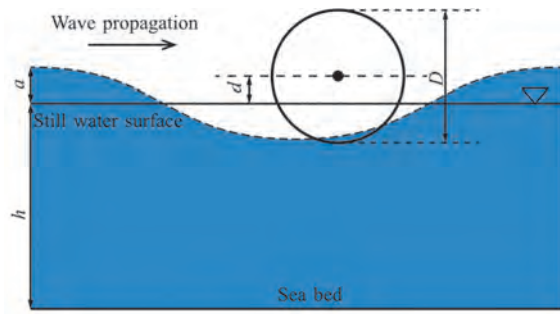

Fig. 23 (Color online) Schematic of the wave interaction with a fixed horizontal cylinder

Table 8 Parameters used in the wave interaction with a fixed horizontal cylinder case

Cases	d'	L'	a'	h'	KC	Re
S1	0	15.62	0.5	8	3.14	2.20×10^6
S2	0	15.62	0.2	8	1.26	1.39×10^6
S3	0.1	15.62	0.2	8	1.26	1.39×10^6

$$\eta = \sum_{i=1}^{n} \frac{H}{2} \cos[k_i x \cos(\beta_i) + k_i y \sin(\beta_i) - \sigma_i t + \varepsilon_i] \quad (20)$$

$$\frac{\partial(\rho\omega)}{\partial t} + \nabla \cdot (\rho \boldsymbol{u}\omega) = \nabla \cdot \left[\left(\mu + \frac{\mu_t}{\tilde{\sigma}_\omega}\right)\nabla\omega\right] + \tilde{C}_\alpha \frac{\omega}{k} P_k -$$

$$\tilde{C}_\beta \rho\omega^2 + 2(1-F_1)\sigma_{\omega 2} \frac{\rho}{\omega} \nabla k \cdot \nabla\omega \quad (21)$$

Since the key variables for coupling are velocity and free surface elevation, the turbulence parameters at the inlet of the OpenFOAM subdomain are simply specified by users. Small values of turbulence parameters are used to comply with the potential flow assumption near the overlapping region and wall functions are used at no-slip wall boundaries. Two irregular wave tests, i.e., two-dimensional wave impacting on a wall and three-dimensional wave impacting on a square, are conducted (See Table 4). Figure 21 shows the surface elevation history recorded at locations in front of the structures. It is seen that including turbulence modeling has negligible effect on the resultant free surface for both the two- and three-dimensional wave tests, which is consistent with the findings in Finnegan and Goggins[33]. Besides, the two-way coupling and OpenFOAM simulations give similar wave forms throughout except slight discrepancies in amplitude at some time points, conforming the effectiveness of the coupling model. Figure 22 shows the y component of vorticity for the wave impacting on a square case from the two-way coupling simulation. The blue surface is the air-water interface in the figure.

Table 7 Parameters of the computational domain for the wave interaction with a fixed horizontal cylinder case

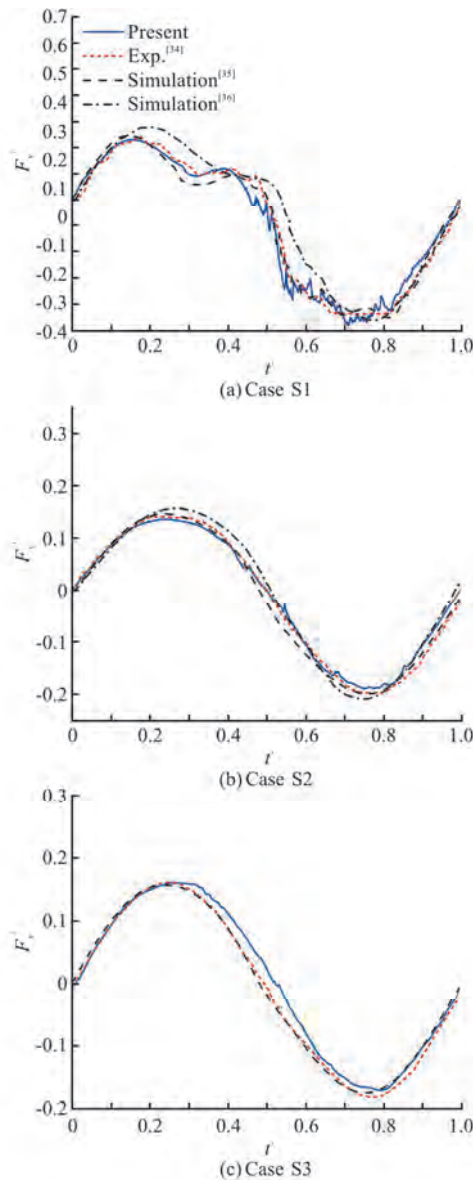| Test	L_P	L_V	L_O	L_R	L_S	$h + h_a$
Wave-cylinder interaction	$80D$	$70D$	$10D$	$5D$	$100.5D$	$12D$

Fig. 24 (Color online) Lift results of the wave interaction with a fixed horizontal cylinder

It is seen that turbulence structures mainly exist in air on top of the free surface while the water is mainly laminar which illustrates the negligible effect of turbulence modeling on the simulation.

3.7 Computational efficiency

The comparison of execution time of the two-way coupling and OpenFOAM simulations for the validation tests is shown in Table 6. All the simulations are run on a single processor titled Intel Core i7-9700KF. It is clearly seen that the coupling procedure saves a considerable amount of time. Based on observations on the simulations, the time savings stem from two sources. One is the replacement of part of the viscous flow domain with the potential flow

domain which possesses a faster computational speed, and the other is that as wave only exists in the potential flow region at the beginning of two-way coupling simulations, the viscous flow model can start running after the wave moving near to the overlapping region, thus saving considerable resources. On the contrary, for pure OpenFOAM simulations, they are started from the beginning for every run.

A further investigation on the efficiency of the two-way coupling strategy reveals that the main time-consuming part of the coupling procedure is the probe of free surface location in the viscous flow domain. For the routines in the two-way coupling implementation, the data transfer from OceanWave3D to OpenFOAM is very fast, but the time spent for probing free surface in OpenFOAM is about three times that of probing velocity and transferring data from OpenFOAM to OceanWave3D. Take the linear wave positive propagation case for example, the free surface and velocity probe routines use 1.6 h out of the total time of 3.1 h, and about 75 percent of that time is spent on the free surface probe. In fact, the used probe function is efficient while the time-consuming property of the routine results from the iterative nature of probing the free surface. The algorithm used for identifying the free surface location is illustrated in Fig. 6. For each probe location, several iterations are needed for finding the alpha value equal to 0.5 where the free surface is defined in VOF. And in the relaxation zone in all present tests, tens of locations need to be probed at each time step, which provides the major source for the time cost in the two-way coupling procedure.

4. Application

4.1 Regular wave interaction with a fixed horizontal cylinder

The first application case is the regular wave interaction with a fixed horizontal cylinder, a schematic of which is shown in Fig. 23. The experimental setup is described in Dixon et al.[34] while numerical reproductions are referred to Deng et al.[35], Ong et al.[36]. In the present two-way coupling simulations, the computational layout follows Fig. 4 with the dimensions given in Table 7, the parameters used in the three test cases are shown in Table 8. The definition of the dimensionless parameters are as follows: $a' = a / D$, where a is the wave amplitude, D is the diameter of the cylinder, $L' = L / D$, where L is the wave length, $d' = d / D$, where d is the submergence depth of the cylinder, $h' = h / D$, where h is the static water depth. The force on the cylinder is computed through integration of pressure and viscous stress over the structural surface as

(a₁) t=0   (b₁) t=0   (c₁) t=0
(a₂) t=0.13   (b₂) t=0.13   (c₂) t=0.13
(a₃) t=0.35   (b₃) t=0.35   (c₃) t=0.35
(a₄) t=0.61   (b₄) t=0.61   (c₄) t=0.61
(a₅) t=0.71   (b₅) t=0.71   (c₅) t=0.71
(a₆) t=1.00   (b₆) t=1.00   (c₆) t=0.13
(a) Deng et al.[35]   (b) One et al.[36]   (c) Present model

Fig. 25 (Color online) Visualization of the wave interaction with a fixed horizontal cylinder case S1

$$F = \int_{\Omega} (-\boldsymbol{n}p + \boldsymbol{n} \cdot \tau)\,\mathrm{d}\Omega \qquad (22)$$

where $\boldsymbol{n}$ refers to the normal vector to the structural surface.

The lift on the cylinder includes the wave inertia force, viscous force and instantaneous buoyancy. The dimensionless lift is calculated as:

$$F_v' = \frac{F_v}{\rho g (\pi D^2 / 4)} \qquad (23)$$

$$F_v = F_{\text{inertia}} + F_{\text{viscous}} + F_{\text{buoyancy}} \qquad (24)$$

$$F_{\text{buoyancy}} = \rho g [V(t) - V_0] \qquad (25)$$

Fig. 26 Schematic of the wave interaction with a T-shaped floating structure

where V_0 and $V(t)$ are the initial and instantaneous displacements of the cylinder.

Table 9 Parameters of the computational domain for the wave interaction with a T-shaped floating structure case

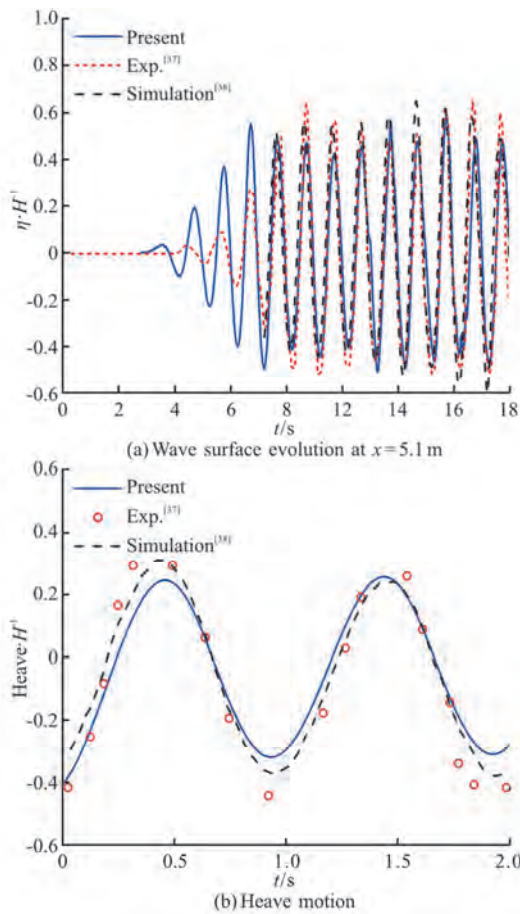| Test	L_P	L_T	L_O	L_R	L_S	$h + h_a$
Wave-structure interaction	5.0 m	10.0 m	1.0 m	1.0 m	7.0 m	1.0 m

Fig. 27 (Color online) Results of the wave interaction with a T-shaped floating structure

Figure 24(a) shows the variation of the dimensionless lift over one wave cycle for case S1 including results from Dixon et al.[34], Deng et al.[35] and Ong et al.[36]. It is seen that the present coupling model predicts well with regards to the existing data. As shown by the experimental data in Fig. 24(a), the lift exhibits two peaks at $t^* = 0.16$, $t^* = 0.40$ respectively in the time range of $t^* < 0.50$ which is related to the wave run-up and overtopping[35], while in $t^* > 0.50$, the lift drops to the lowest value at about $t^* = 0.7$. These key features in lift are well captured by the coupling model. Figure 25 is a visual comparison of the free surface evolution during one wave period. It is further confirmed that the wave behaviors predicted by the two-way coupling model agree well with Deng et al.[35], Ong et al.[36], especially the wave breaking pattern and position. It is shown in Fig. 25 that the wave crest moves toward the cylinder from $t^* = 0$ to $t^* = 0.13$ corresponding to the rise in lift in Fig. 24(a), and the wave reflection is displayed at $t^* = 0.13$. At the time around $t^* = 0.35$, wave run-up and overtopping occur such that two lift peaks form as

explained in Deng et al.[35]. At $t^* = 0.61$, $t^* = 0.71$, the wave tough approaches the cylinder making the structure standing above the instantaneous water surface that leads to the reduction in lift.

Figure 24(b) shows the lift results for case S2. Since the wave overtopping does not emerge for this gentle wave, the lift varies generally in a sinusoidal manner with slight nonlinearity. All the results shown in Fig. 24(b) match well, confirming the reliability of the coupling model. Figure 24(c) shows the lift results for case S3. Due to that the cylinder is elevated $0.1D$ upwards, the interaction between the wave and cylinder weakens. Again, the agreement in lift is good.

4.2 *Regular wave interaction with a T-shaped floating structure*

The coupling model is applied to a more complicated case, i.e., regular wave interaction with a T-shaped floating structure, a schematic of which is shown in Fig. 26. Experiment and simulation of the case are referred to Zhao and Hu[37], Chen et al.[38], respectively. The experiments were conducted in a narrow wave flume with dimensions 18.0 m×0.3 m×0.7 m at Research Institute for Applied Mechanics, Kyushu University[37]. The water depth is 0.4 m and the incident wave is chosen to be $H = 0.062 \, \text{m}$, $T = 1.0 \, \text{s}$. The T-shaped floating object is placed at 7.0 m from the wave inlet, and is only allowed to move in heave and pitch. The mass of the structure is 15 kg and the moment of inertia in pitch is 0.3417 kg·m^2 as shown in Fig. 26. A rotational joint which deviates from the center of mass is fixed to force the structure to pitch around it. In the present simulations, the computational domain is slightly shortened in length comparing to the experiments and has the layout assembling Fig. 4 with the dimensions given in Table 9.

Figures 27(a), 27(b) show the wave surface evolution at $x = 5.1 \, \text{m}$ and heave motion of the structure, respectively. It is seen that the free surface agrees well with the data in literature while the predicted motion of the structure deviates slightly from the measurement. It is noted that the moment of inertia in pitch used in the present research is calculated based on the data given in Chen et al.[38], which may affect the agreement of the results. Nevertheless, the trend of the heave motion generally matches the experiments. Figure 28 visualizes the free surface and motion of the structure. It is shown that the predictions agree well between the present model and the simulations in Chen et al.[38]. In comparison to the experimental results in Zhao and Hu[37], the magnitudes of wave run-up and structural motion are slightly reduced.
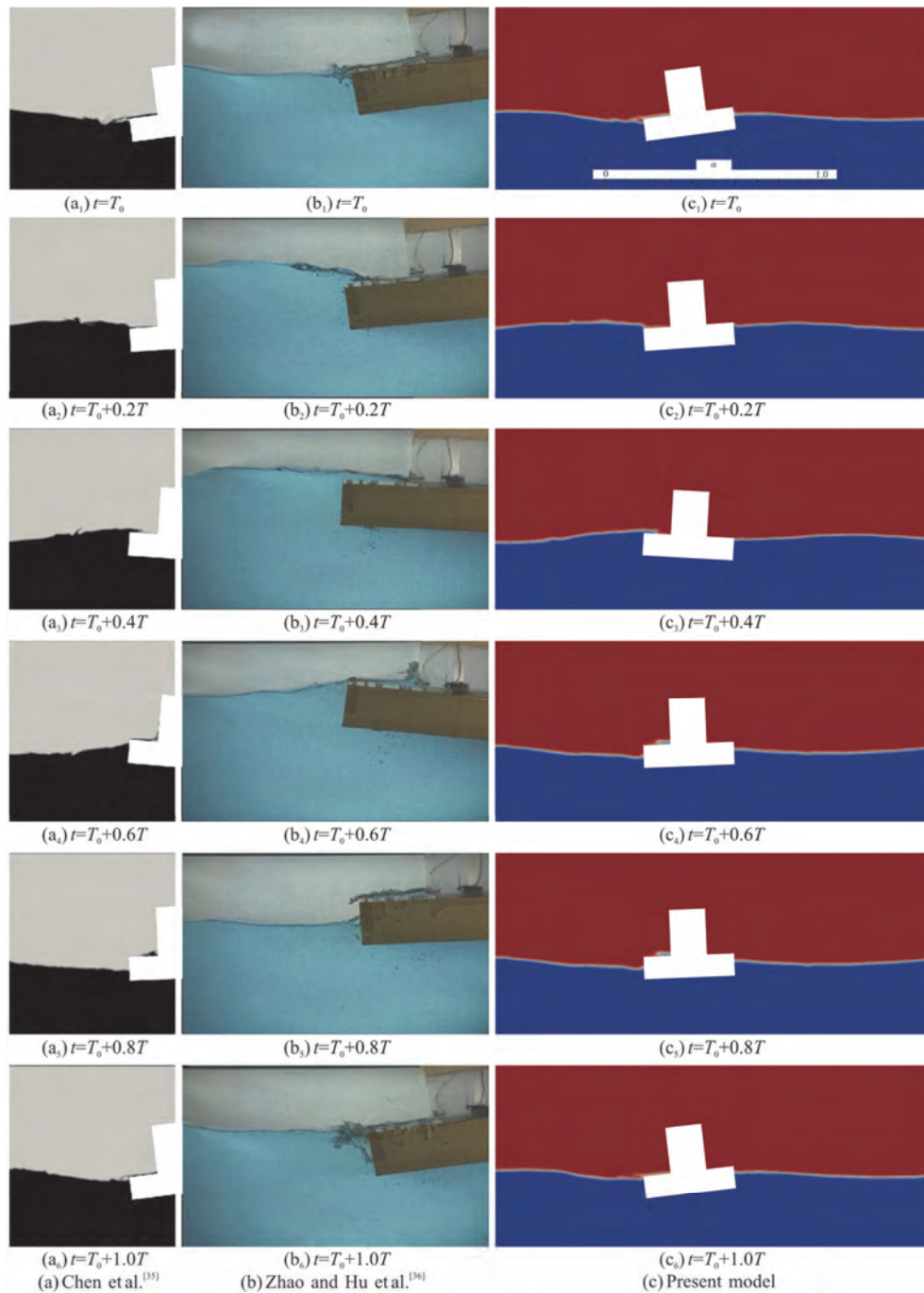
Fig. 28 (Color online) Visualization of the wave interaction with a T-shaped floating structure

5. Conclusions

In this paper, an innovative two-way coupling strategy on potential and viscous flow models was proposed. The used potential and viscous flow models were the open source OceanWave3D, OpenFOAM-v2012, respectively. The two-way coupling strategy utilized the ghost point approach in OceanWave3D, thus avoiding calculating velocity potential when transferring kinematic data from OceanWave3D to OpenFOAM. To prevent computational divergence, a relaxation zone is used at the outlet in the OceanWave3D domain for imposing the free surface elevation and velocity probed in OpenFOAM. The velocity potential in the relaxation zone is indirectly built upon its temporal variation which is calculated by the free surface boundary condition equation using the probed velocity data. Two- and three-dimensional validation tests, including regular, irregular, and multi-directional irregular waves, were conducted.

Results show that the new two-way coupling strategy is robust in transferring data between OceanWave3D, OpenFOAM, thus providing an effective tool for wave structure interaction simulations.

RANS turbulence model has been included in the coupling scheme and it is shown to have negligible effect on the test results, revealing the laminar property of the wave field. Moreover, efficiency analysis of the proposed coupling strategy indicates that dramatic time savings are achieved with respect to individual OpenFOAM simulations. Two sources for the efficiency gains are identified including replacement of part of the viscous flow domain with the potential flow domain and shortened run time of the viscous flow model due to no induced wave motion at the beginning of coupling simulations. It is also found that the main time-consuming part of the coupling procedure is the probe of free surface location in the viscous flow domain which utilizes an iterative algorithm. The used probe function is efficient while the iterative nature of probing the free surface results in the time-consuming property of the free surface probe routine.

Moreover, the two-way coupling model has been applied to two wave-structure interaction problems against published experiments, including the wave interaction with a fixed horizontal cylinder and a T-shaped floating structure. In both problems, comparisons in key quantities and visualization show good agreements between the proposed model and existing data, thus further confirming the reliability of the coupling approach.

References

[1] Yan H., Liu Y. An efficient high-order boundary element method for nonlinear wave-wave and wave-body interactions [J]. *Journal of Computational Physics*, 2011, 230(2): 402-424.

[2] Chen Y. L., Hsiao S. C., Generation of 3D water waves using mass source wavemaker applied to Navier-Stokes model [J]. *Coastal Engineering*, 2016, 109: 76-95.

[3] Higuera P., Lara J. L., Losada I. J. Realistic wave generation and active wave absorption for Navier-Stokes models: Application to OpenFOAM® [J]. *Coastal Engineering*, 2013, 71: 102-118.

[4] Higuera P., Losada I. J., Lara J. L. Three-dimensional numerical wave generation with moving boundaries [J]. *Coastal Engineering*, 2015, 101: 35-47.

[5] Jacobsen N. G., Fuhrman D. R., Fredsoe J. A wave generation toolbox for the open-source CFD library: OpenFoam® [J]. *International Journal for Numerical Methods in Fluids*, 2012, 70(9): 1073-1088.

[6] Xie Z., Lu L., Stoesser T. et al. Numerical simulation of three-dimensional breaking waves and its interaction with a vertical circular cylinder [J]. *Journal of Hydrodynamics*, 2017, 29(5): 800-804.

[7] Wang J. H., Zhao W. W., Wan D. C. Development of naoe-FOAM-SJTU solver based on OpenFOAM for marine hydrodynamics [J]. *Journal of Hydrodynamics*, 2019, 31(1): 1-20.

[8] Ferrant P., Gentaz L., Alessandrini B. et al. A potential/RANSE approach for regular water wave diffraction about 2-D structures [J]. *Ship Technology Research*, 2003, 50(4): 165-171.

[9] Gentaz L., Luquet R., Alessandrini B. et al. Numerical simulation of the 3D viscous flow around a vertical cylinder in non-linear waves using an explicit incident wave model [C]. *23rd International Conference on Offshore Mechanics and Arctic Engineering*, Vancouver, Canada, 2004.

[10] Vukcevic V., Jasak H., Malenica S. Decomposition model for naval hydrodynamic applications, Part I: Computational method [J]. *Ocean Engineering*, 2016, 121: 37-46.

[11] Li Z., Bouscasse B., Gentaz L. et al. Progress in coupling potential wave models and two-phase solvers with the SWENSE methodology [C]. *Offshore Geotechnics; Honoring Symposium for Professor Bernard Molin on Marine and Offshore Hydrodynamics*, Madrid, Spain, 2018.

[12] Choi Y., Bouscasse B., Seng S. et al. Generation of regular and irregular waves in Navier-Stokes CFD solvers by matching with the nonlinear potential wave solution at the boundaries [C]. *ASME 37th International Conference on Ocean, Offshore and Arctic Engineering*, Madrid, Spain, 2018.

[13] Gatin I., Vukcevic V., Jasak H. A framework for efficient irregular wave simulations using higher order spectral method coupled with viscous two phase model [J]. *Journal of Ocean Engineering and Science*, 2017, 2(4): 253-267.

[14] Paulsen B. T., Bredmose H., Bingham H. B. An efficient domain decomposition strategy for wave loads on surface piercing circular cylinders [J]. *Coastal Engineering*, 2014, 86(17): 57-76.

[15] Zhuang Y., Wan D. C. Parametric study of a new HOS-CFD coupling method [J]. *Journal of Hydrodynamics*, 2021, 33(1): 43-54.

[16] Iafrati A., Campana E. F. A domain decomposition approach to compute wave breaking (wave-breaking flows) [J]. *International Journal for Numerical Methods in Fluids*, 2003, 41(4): 419-445.

[17] Zhang Y., Peszynska M., Yim S. C., Coupling of viscous and potential flow models with free surface for near and far field wave propagation [J]. *International Journal of Numerical Analysis and Modeling*, 2013, 4(3): 256-82.

[18] Zhang Y., Yim S. C., Pin F. D. A nonoverlapping heterogeneous domain decomposition method for three-dimensional gravity wave impact problems [J]. *Computers and Fluids*, 2015, 106: 154-170.

[19] Colicchio G., Greco M., Faltinsen O. M. A BEM-level set domain-decomposition strategy for non-linear and fragmented interfacial flows [J]. *International Journal for Numerical Methods in Engineering*, 2006, 67(10): 1385-1419.

[20] Kim S. H., Yamashiro M., Yoshida A. A simple two-way coupling method of BEM and VOF model for random wave calculations [J]. *Coastal Engineering*, 2010, 57(11): 1018-1028.

[21] Hamilton J. A., Yeung R. W. Viscous and inviscid matching of three-dimensional free-surface flows utilizing shell functions [J]. *Journal of Engineering Mathematics*, 2011, 70(1): 43-66.

[22] Ferrer P. J. M., Causon D. M., Qian L. et al. A multi-region coupling scheme for compressible and incom-

pressible flow solvers for two-phase flow in a numerical wave tank [J]. *Computers and Fluids*, 2016, 125: 116-129.

[23] Di Paolo B., Lara J. L., Barajas G. et al. Wave and structure interaction using multi-domain couplings for Navier-Stokes solvers in OpenFOAM®. Part I: Implementation and validation [J]. *Coastal Engineering*, 2021, 164: 103799.

[24] Di Paolo B., Lara J. L., Barajas G. et al. Waves and structure interaction using multi-domain couplings for Navier-Stokes solvers in OpenFOAM®. Part II: Validation and application to complex cases [J]. *Coastal Engineering*, 2021, 164: 103818.

[25] Stelling G., Zijlema M. An accurate and efficient finite-difference algorithm for non-hydrostatic free-surface flow with application to wave propagation [J]. *International Journal for Numerical Methods in Fluids*, 2003, 43(1): 1-23.

[26] Engsig-Karup A. P., Bingham H. B., Lindberg O. An efficient flexible-order model for 3D nonlinear water waves [J]. *Journal of Computational Physics*, 2009, 228(6): 2100-2118.

[27] Ducrozet G., Bonnefoy F., Touze D. L. et al. A modified high-order spectral method for wavemaker modeling in a numerical wave tank [J]. *European Journal of Mechanics B-Fluids*, 2012, 34: 19-34.

[28] Duz B., Bunnik T., Kapsenberg G. et al. Numerical simulation of nonlinear free surface water waves: Coupling of a potential flow solver to a URANS/VOF code [C]. *ASME 35th International Conference on Ocean, Offshore and Arctic Engineering*, Busan, Korea, 2016.

[29] Bingham H. B., Zhang H. On the accuracy of finite-difference solutions for nonlinear water waves [J]. *Journal of Engineering Mathematics*, 2007, 58(1): 211-228.

[30] Berberovic E., van Hinsberg N. P., Jakirlic S. et al. Drop impact onto a liquid layer of finite thickness: Dynamics of the cavity evolution [J]. *Physical Review E*, 2009, 79(3): 36306-36306.

[31] Zhong W., Yim S. C., Deng L. Vortex shedding patterns past a rectangular cylinder near a free surface [J]. *Ocean Engineering*, 2020, 200: 107049.

[32] Zhong W., Yim S. C., Deng L. Reynolds-number effect on flow past a rectangular cylinder in the presence of a free surface [J]. *Ocean Engineering*, 2020, 216: 107865.

[33] Finnegan W., Goggins J. Numerical simulation of linear water waves and wave-structure interaction [J]. *Ocean Engineering*, 2012, 43(4): 23-31.

[34] Dixon A. G., Salter S. H., Greated C. A. Wave forces on partially submerged cylinders [J]. *Journal of the Waterway, Port, Coastal and Ocean Division*, 1979, 105(4): 421-438.

[35] Deng X., Liu S., Ong M. C. et al. Numerical simulations of free-surface waves past two vertically aligned horizontal circular cylinders [J]. *Ocean Engineering*, 2019, 172: 550-561.

[36] Ong M. C., Kamath A., Bihs H. et al. Numerical simulation of free-surface waves past two semi-submerged horizontal circular cylinders in tandem [J]. *Marine Structures*, 2017, 52: 1-14.

[37] Zhao X., Hu C. Numerical and experimental study on a 2-D floating body under extreme wave conditions [J]. *Applied Ocean Research*, 2012, 35: 1-13.

[38] Chen H., Qian L., Ma Z. et al. Application of an overset mesh based numerical wave tank for modelling realistic free-surface hydrodynamic problems [J]. *Ocean Engineering*, 2019, 176: 97-117.